
PRISM : A Geometric Risk Bound that Decomposes Drift into Scale, Shape, and Head

Chieh-Yen Lin¹ Shao-Hua Sun^{1,2}

¹Appier AI Research, ²National Taiwan University
cylin@appier.com

Abstract

Comparing post-training LLM variants—quantized, LoRA-adapted, distilled—needs a diagnostic that pinpoints *how* the variant has drifted, not just *that* it has; existing similarity scores (CKA, SVCCA) flag degradation without linking to risk or mechanism. We propose **PRISM** (Proxy Risk Inference via Structural Mapping), exploiting LLMs’ linear head and empirically near-isometric backbone to derive a closed-form upper bound on the cross-entropy risk gap $|\mathcal{R}_T - \mathcal{R}_P|$, calibrated for variant ranking, that decomposes drift into three independently measurable axes: *scale mismatch*, *shape mismatch*, and a *head divergence*. Each axis maps to a distinct failure mode (shape distortion at low-bit quantization, scale separability under LoRA forgetting, head divergence at GGUF k-quant), so the dominant axis points to a remediation direction rather than a flag. Because the shape term is differentiable, the same geometry doubles as a training-time regularizer against catastrophic forgetting. Across two model families and five benchmarks, PRISM ranks variants with mean Spearman $r_s=0.820$ (PTQ) and 0.831 (LoRA forgetting), and the axis-guided shape regularizer outperforms experience replay in aggregate at mitigating downstream forgetting.

1 Introduction

As large language models (LLMs) move from pre-training to deployment, a new bottleneck emerges: a single base model now produces many post-training variants—quantized (GPTQ [1], GGUF, BitsAndBytes [2]), LoRA-adapted [3], or distilled [4]—that must be evaluated before release [5, 6]. Existing evaluation largely relies on aggregate accuracy or perplexity, which can reveal that a variant has degraded but not *why*. As a result, developers often resort to costly trial-and-error when debugging low-bit quantization failures, catastrophic forgetting, or prediction-head corruption. What is missing is a diagnostic that not only predicts degradation, but also identifies which component of the model has drifted from the base checkpoint.

A natural alternative is to compare internal representations directly. Prior representational similarity methods—SVCCA [7], CKA [8], and generalized shape metrics—summarize two feature matrices with a single alignment score, which is descriptive but not diagnostic. More fundamentally, lifting any such score into a deployment-time risk bound faces three obstacles: (i) no prior similarity has been tied to downstream cross-entropy risk on the deployed prediction head [9–11]; (ii) cross-entropy is Lipschitz in features, but the naive constant scales with the head’s full spectral norm and is uninformative at LLM vocabulary scale ($V \sim 10^5$); and (iii) a usable diagnostic must further decompose the bound into geometrically interpretable axes that map to distinct failure mechanisms.

Our key insight is that two structural properties of modern LLMs jointly resolve all three obstacles. The linear $\mathbb{1}_m$ head over a non-linear backbone lets us derive a sharper Lipschitz constant tied to pairwise token-embedding distances rather than the head’s spectral norm, keeping the bound informative at LLM vocabulary scale (Sec. 3.2). With the near-isometry of hidden representations across related LLMs [12, 13], an orthogonal alignment yields a Procrustes residual that decomposes

Preprint.

the feature error *exactly* into scale and shape axes. Together with a covariance-weighted head-side term, these produce **PRISM** (Proxy Risk Inference via Structural Mapping; Fig. 1), a closed-form upper bound on the cross-entropy risk gap between a target model and its variant.

PRISM exposes three diagnostic axes: *scale mismatch* $\Delta\rho$ (activation magnitude collapse), *shape mismatch* $1 - \Omega$ (feature-geometry distortion), and a covariance-weighted *head discrepancy* γ (prediction-head divergence). Unlike scalar similarity scores, these axes correspond to distinct empirical failure modes: low-bit quantization primarily induces shape distortion, LoRA fine-tuning yields activation scale separability, and output-projection quantization inflates head divergence.

Beyond post-hoc diagnosis, PRISM also provides a training signal. Under frozen-head LoRA fine-tuning, the head discrepancy term vanishes, making the differentiable shape term a clean regularization target for backbone drift. This allows us to regularize fine-tuning directly by penalizing feature-geometry distortion, reducing catastrophic forgetting without replay (Sec. 5.4). Empirically, across Llama-, Qwen-, Ministral-, and DeepSeek-based variants and five benchmarks, PRISM consistently tracks degradation across both post-training quantization (PTQ) and LoRA fine-tuning. The bound achieves mean Spearman correlations of 0.820 for quantized variants and 0.831 for LoRA forgetting; beyond ranking, its axes separate distinct failure modes. Moreover, the proposed axis-guided shape regularizer outperforms replay-based baselines in mitigating forgetting.

Our contributions are threefold.

1. **Theory: a closed-form CE risk bound with three diagnostic axes.** $|\mathcal{R}_T - \mathcal{R}_P|$ admits a closed-form upper bound as a sum of three axes: scale $(\Delta\rho)^2$ and shape $2\rho_T\rho_P(1-\Omega)$ (from an exact Procrustes residual decomposition), plus a covariance-weighted head-discrepancy term (Theorem 1; Fig. 1).
2. **Framework: a unified diagnostic that doubles as a training objective.** Computed from features and head weights alone, the bound applies across both PTQ and frozen-head LoRA; the differentiable trace form Ω further turns it into a training-time regularizer against catastrophic forgetting (Sec. 5.4).
3. **Empirical: rank-consistent across both settings, with axis-level localization.** On Llama and Qwen (Ministral, DeepSeek in Appendix F.3) over five benchmarks, the bound ranks PTQ variants ($r_s=0.820$) and LoRA checkpoints ($r_s=0.831$) consistently (*predictiveness*); its axes separate failure modes—shape distortion at Q2/Q3 PTQ, scale separability under cross-task LoRA drift, head divergence at Qwen3 Q6_K/Q8_0 (*decomposability*); and an axis-guided shape regularizer outperforms experience replay in aggregate at mitigating downstream forgetting (*actionability*).

2 Related work

Representational similarity and Procrustes shape metrics. Representational similarity statistics—SVCCA [7], CKA [8], and the generalized shape metrics framework [14]—measure geometric resemblance between activation matrices, but their link to downstream behavior remains an open problem [9–11]; a recent decodability bound [15] reaches downstream via whitened kernels and newly-trained linear probes rather than the deployed prediction heads. The Linear Representation Hypothesis [12] and empirical relative-representation isometry across same-family encoders [13] together motivate restricting alignment to the orthogonal group, and the Platonic Representation Hypothesis [16] corroborates same-family shared geometry. PRISM lifts the Procrustes residual into a closed-form CE risk bound on the deployed head; the resulting bound splits into separately measurable scale, shape, and head components (Sec. 3).

Post-training quantization and its evaluation. Post-training quantization spans calibration-based methods (GPTQ [1], second-order reconstruction) and weight-only schemes (GGUF k-quants, BitsAndBytes [2]), with low-bit performance often constrained by activation outliers [17]. Existing cheap diagnostics—layer-wise reconstruction loss or weight quantization error—are indirect proxies that do not account for nonlinear error accumulation through the full network. PRISM, in contrast, measures the resulting drift end-to-end on the deployed model in a single forward pass (Sec. 5.2).

Catastrophic forgetting under parameter-efficient fine-tuning. LoRA fine-tuning [3] risks catastrophic forgetting of pre-training knowledge, even with a frozen `lm_head`. Existing remedies fall into two families: weight-space constraints (EWC [18]) and data-space rehearsal (experience

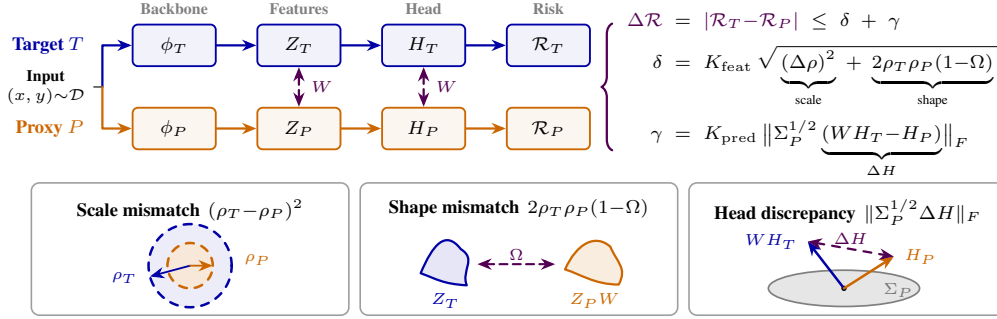


Figure 1: **PRISM (Proxy Risk Inference via Structural Mapping) decomposition of the risk gap.** For any orthogonal alignment $W \in \mathcal{O}(d)$, the cross-entropy risk gap $|\mathcal{R}_T - \mathcal{R}_P|$ is bounded (Thm. 1) by a feature alignment error δ —decomposed exactly into *scale mismatch* $(\Delta\rho)^2$ and *shape mismatch* $2\rho_T\rho_P(1-\Omega)$ (Prop. 1)—plus a head discrepancy $\gamma = K_{\text{pred}}\|\Sigma_P^{1/2}\Delta H\|_F$ where $\Delta H = WH_T - H_P$. The main text uses the identity alignment $W=I$ (Ω), under which γ vanishes whenever $H_T = H_P$ (frozen-head LoRA, FP16-head PTQ); both $W=I$ and the Procrustes-optimal $W=W_N$ yield strong rank correlations (Sec. 5.5). Each axis localizes a distinct empirical regime: shape distortion at low-bit PTQ, head divergence at GGUF k-quant tiers that quantize `lm_head`, and scale-axis separability under LoRA forgetting (Sec. 5.3).

replay). PRISM’s shape regularizer adds a third option—a feature-geometry constraint identifiable from the bound’s decomposition: feature-manifold drift (Ω , $\Delta\rho$) relative to the frozen base bounds the downstream risk gap and is usable as a post-hoc diagnostic and a training-time penalty (Sec. 3.5).

Efficient evaluation and performance forecasting. Scaling laws [19, 20] predict aggregate loss but not variant-specific degradation; efficient-evaluation subsets [21, 22] preserve variant orderings without explaining them; weak-to-strong generalization [23] targets label generation rather than risk estimation. PRISM instead bounds the variant-vs-base risk gap directly from a feature comparison—not relying on benchmark labels or aggregate-loss extrapolation (Sec. 3).

3 A geometric bound on the cross-entropy risk gap

PRISM (Proxy Risk Inference via Structural Mapping)—developed in this section—is a closed-form upper bound on the cross-entropy risk gap $|\mathcal{R}_T - \mathcal{R}_P|$ that decomposes into three diagnostic axes (scale, shape, head). We build it from two structural properties of LLMs: a linear `lm_head` on a non-linear backbone, and the Linear Representation Hypothesis.

3.1 Setup

Let T be a *Target model* (e.g., a full-precision base) and P a *Proxy model* (e.g., a quantized or fine-tuned variant), sharing hidden dimension d . Each model factors into a Transformer backbone $\phi_M : \mathcal{X} \rightarrow \mathbb{R}^d$ followed by a linear prediction head $H_M \in \mathbb{R}^{d \times V}$ (the `lm_head`, vocabulary size V). The risk of M under data distribution \mathcal{D} is the cross-entropy expectation

$$\mathcal{R}_M = \mathbb{E}_{(x,y) \sim \mathcal{D}}[\ell(\phi_M(x)H_M, y)], \quad \ell(v, y) = -v_y + \log \sum_{j=1}^V e^{v_j}, \quad v \in \mathbb{R}^V. \quad (1)$$

Stacking ϕ_M outputs on shared inputs as rows, we form $Z_T, Z_P \in \mathbb{R}^{n \times d}$ and define the RMS feature scale $\rho_M = \|Z_M\|_F / \sqrt{n}$ and the empirical (uncentered) covariance $\Sigma_P = Z_P^\top Z_P / n$. The empirical isometry across model representations [13], consistent with the Linear Representation Hypothesis [12], motivates restricting attention to orthogonal alignments $W \in \mathcal{O}(d)$ between the two backbones; the PRISM bound (Theorem 1) holds for any such W , with alignment quality determining how tight the bound is in practice.

3.2 The unified risk bound

To bound $|\mathcal{R}_T - \mathcal{R}_P|$ we introduce a hybrid risk $\mathcal{R}_{P \rightarrow T} := \mathbb{E}[\ell(\phi_P(x)W \cdot H_T, y)]$ that evaluates the target’s head on the proxy’s aligned features. The triangle inequality $|\mathcal{R}_T - \mathcal{R}_P| \leq |\mathcal{R}_T - \mathcal{R}_{P \rightarrow T}| + |\mathcal{R}_{P \rightarrow T} - \mathcal{R}_P|$ splits the gap into two components, each upper-bounded by a closed-form geometric quantity: a *feature alignment error* δ and a *head discrepancy* γ (full derivations in Appendix A).

Feature error δ . The cross-entropy loss is Lipschitz in features with constant $K_{\text{feat}} = \max_{j,k} \|h_{T,j} - h_{T,k}\|_2$, where $h_{T,j}$ is the j -th column of H_T (simplex polarization, Appendix A.3; substantially tighter than the naive spectral bound $\sqrt{2}\|H_T\|_2$ that scales with vocabulary). The alignment residual $\|Z_T - Z_P W\|_F^2/n$ admits an exact identity for every orthogonal W :

Proposition 1 (Exact Scale–Shape Decomposition). *For any $W \in \mathcal{O}(d)$,*

$$\frac{1}{n} \|Z_T - Z_P W\|_F^2 = \underbrace{(\rho_T - \rho_P)^2}_{\text{Scale Mismatch } (\Delta\rho)^2} + \underbrace{2\rho_T\rho_P(1 - \Omega_W)}_{\text{Shape Mismatch}}, \quad (2)$$

where Ω_W is the trace Procrustes similarity:

$$\Omega_W(Z_T, Z_P) := \frac{\text{Tr}(Z_T^\top Z_P W)}{\|Z_T\|_F \|Z_P\|_F} \in [-1, 1]. \quad (3)$$

Combined with the Lipschitz bound (Appendix A), we define

$$\delta := K_{\text{feat}} \sqrt{(\rho_T - \rho_P)^2 + 2\rho_T\rho_P(1 - \Omega_W)}, \quad |\mathcal{R}_T - \mathcal{R}_{P \rightarrow T}| \leq \delta. \quad (4)$$

Head error γ . Let $\Delta H := WH_T - H_P$ for the alignment W ; we define $\gamma := K_{\text{pred}} \|\Sigma_P^{1/2} \Delta H\|_F$ with $K_{\text{pred}} \leq \sqrt{2}$ (Appendix A.5), so that $|\mathcal{R}_{P \rightarrow T} - \mathcal{R}_P| \leq \gamma$. The covariance weighting $\Sigma_P^{1/2}$ ensures that only head misalignment in the *active subspace* (directions where the data has support) contributes to γ .

Theorem 1 (Unified Risk Bound). *For any $W \in \mathcal{O}(d)$,*

$$|\mathcal{R}_T - \mathcal{R}_P| \leq \mathcal{B} := \underbrace{K_{\text{feat}} \sqrt{(\rho_T - \rho_P)^2 + 2\rho_T\rho_P(1 - \Omega_W)}}_{\delta: \text{feature alignment error}} + \underbrace{K_{\text{pred}} \|\Sigma_P^{1/2} (WH_T - H_P)\|_F}_{\gamma: \text{head discrepancy}}. \quad (5)$$

We refer to $\mathcal{B} = \delta + \gamma$ as the PRISM bound.

3.3 Three diagnostic axes

Theorem 1 (illustrated in Fig. 1) decomposes the risk gap along three *independently measurable* axes, each attached to a distinct failure mode of the proxy.

Scale mismatch $\Delta\rho$. Divergence in activation magnitude directly amplifies the feature error. Aggressive bit-width reduction clips activation outliers [2, 17], shrinking $\rho_P < \rho_T$; the scale axis isolates this *scale collapse*.

Shape mismatch $1 - \Omega_W$. The shape term captures geometric distortion of the feature manifold beyond scale. A drop in Ω_W signals that the relative arrangement of token representations has been corrupted—what we term *structural distortion*.

Head divergence $\|\Sigma_P^{1/2} (WH_T - H_P)\|_F$. The head term quantifies how differently the prediction heads interpret features, weighted by Σ_P so that only directions where the data has support contribute.

PRISM applies for any orthogonal alignment. Theorem 1 holds for every $W \in \mathcal{O}(d)$, yielding a family $\{\Omega_W\}$ of similarity scores. We evaluate two natural specializations: the trace form $\Omega := \Omega_{W=I}$ (used as the main text default) and the Procrustes-optimal nuclear form $\Omega_N := \Omega_{W=W_N}$ (ablation in Sec. 5.5; full derivation in Appendix B). $W=W_N$ minimizes the alignment residual but introduces nonzero γ when $H_T \approx H_P$ and requires per-step SVD; $W=I$ keeps γ at its minimum—vanishing when $H_T=H_P$ (frozen-head LoRA, FP16-head PTQ; GGUF k-quant keeps $\gamma>0$)—and is directly differentiable, enabling the regularizer of Sec. 3.5. Both yield strong rank correlations (Sec. 5.5); the choice is primarily design-driven.

3.4 Formal extension to autoregressive generation

The bound applies unchanged to sequence-level generation. For a sequence (c, y) with context c and target continuation $y = (y_1, \dots, y_{|y|})$, the autoregressive risk is

$$\mathcal{R}_M^{\text{AR}} = \mathbb{E}_{(c,y) \sim \mathcal{D}} \left[\frac{1}{|y|} \sum_{\tau=1}^{|y|} \ell(\phi_M(c, y_{<\tau}) \cdot H_M, y_\tau) \right]. \quad (6)$$

Under teacher forcing, the $|y|$ token-level features $\phi_M(c, y_{<\tau})$ of a sequence are extracted in a single forward pass and stacked into $Z_M^{\text{AR}} \in \mathbb{R}^{|y| \times d}$; Theorem 1 then applies directly to $(Z_T^{\text{AR}}, Z_P^{\text{AR}})$. The full corollary is in Appendix D.

3.5 From diagnostic to training: shape regularization

LoRA fine-tuning drives the backbone shape away from its base: $\Omega(Z_0, Z_t)$ drops as training proceeds, and—because the head is frozen—the full risk gap between base θ_0 and checkpoint θ_t reduces to backbone drift alone,

$$|\mathcal{R}_0 - \mathcal{R}_t| \leq K_{\text{feat}} \sqrt{(\rho_0 - \rho_t)^2 + 2\rho_0\rho_t(1 - \Omega)}. \quad (7)$$

Constraining shape should therefore reduce backbone drift and mitigate catastrophic forgetting on downstream tasks. Since $1 - \Omega$ is differentiable in Z_t , we augment the fine-tuning objective with a *shape regularizer*—a penalty on $1 - \Omega$:

$$L_{\text{total}} = \underbrace{L_{\text{CE}}(\theta_t; \mathcal{D}_{\text{FT}})}_{\text{task loss}} + \lambda (1 - \Omega(Z_0^{\text{ref}}, Z_t^{\text{ref}})), \quad (8)$$

where $Z_0^{\text{ref}}, Z_t^{\text{ref}}$ are base and current feature matrices on a fixed reference set (training schedule in Sec. 5.1); empirical effect is validated in Sec. 5.4.

4 Applications: post-training quantization and LoRA forgetting

The Unified Risk Bound (Theorem 1; Fig. 1) applies to two LLM lifecycle settings: post-training quantization (may engage all three axes) and frozen-head LoRA fine-tuning (backbone drift alone).

Quantization quality estimation. Target T is the BF16 base model and proxy P is the quantized variant. Weight-only PTQ perturbs weights without applying any basis transformation, so $W=I$ is the natural alignment; the head term γ enters when the protocol also quantizes `lm_head` (GGUF k-quant) and vanishes otherwise (GPTQ, BnB).

Geometric monitoring of catastrophic forgetting. Target $T=\theta_0$ is the frozen base model and proxy $P=\theta_t$ a fine-tuned checkpoint, both evaluated on benchmarks *distinct* from the fine-tuning task so that $|\mathcal{R}_T - \mathcal{R}_P|$ captures catastrophic forgetting. Standard LoRA [3] keeps `lm_head` frozen, so $\gamma=0$ and forgetting reduces to *backbone geometric drift* $(\Delta\rho, 1-\Omega)$; the shape regularizer of Sec. 3.5 penalizes the shape term directly.

5 Experiments

We organize the experiments around three claims: **Predictiveness**—the bound tracks $|\Delta\mathcal{R}|$ in rank order across both PTQ and LoRA variants (Sec. 5.2); **Decomposability**—its three axes localize three qualitatively distinct empirical failure modes (Sec. 5.3); and **Actionability**—the differentiable shape arm doubles as a training-time regularizer that suppresses catastrophic forgetting (Sec. 5.4). Sec. 5.5 closes with a component-wise ablation.

5.1 Experimental setup

Models. The main analysis spans two model families: Llama-3.1-8B [5] and Qwen3-8B [6]; PTQ replications on Ministral-3-8B [24], DeepSeek-R1-Distill-Llama-8B [25], and three instruction-tuned counterparts (seven 8B families total) are in Appendix F.3.

Quantization protocols. Three PTQ families across bit-widths 2–8, spanning basic rounding to calibration-based compensation: **GGUF** (round-to-nearest, Q2_K–Q8_0), **GPTQ** [1] (4-bit, second-order reconstruction), and **BitsAndBytes** [2] (INT8, NF4, FP4).

Fine-tuning tasks. LoRA fine-tunes on **TruthfulQA** [26] (factual grounding) and **BBQ** [27] (Bias Benchmark for QA, social-context reasoning)—two tasks with contrasting drift geometries (Sec. 5.3). Downstream forgetting is measured on benchmarks disjoint from both fine-tuning tasks.

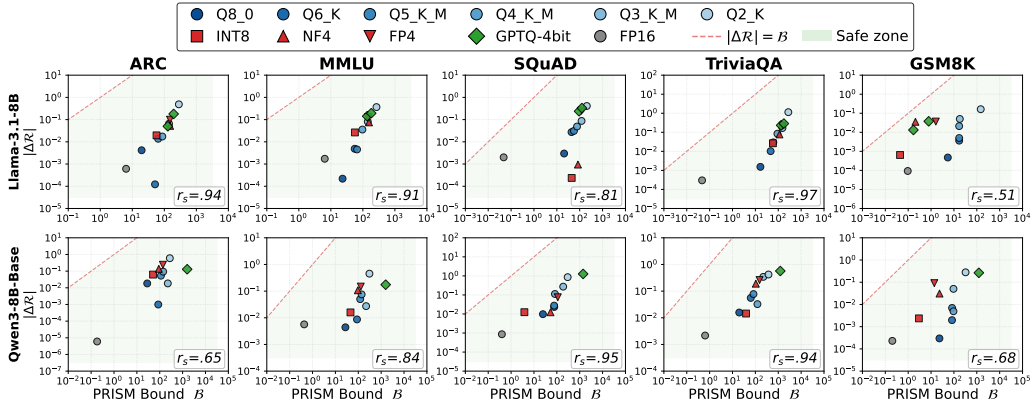


Figure 2: **The PRISM bound \mathcal{B} tracks the empirical risk gap across two model families and five benchmarks.** Each subplot scatters the PRISM bound \mathcal{B} (x-axis, log) against the empirical cross-entropy risk gap $|\Delta\mathcal{R}|$ (y-axis, log). Each point is one quantization variant; colors denote PTQ family (GGUF / GPTQ / BitsAndBytes). Rows: Llama-3.1-8B, Qwen3-8B. Columns: ARC, MMLU, SQuAD, TriviaQA, GSM8K. Per-subplot Spearman r_s is annotated in each panel (mean $r_s \approx 0.82$ across the 2×5 grid; per-component breakdown in Sec. 5.5); the red dashed $y=x$ line marks bound tightness, and the **green shaded region below it** is the safe zone where the bound provably holds. Replication on Ministral-3-8B and DeepSeek-R1-Distill-Llama-8B: Fig. 5 (Appendix F).

Table 1: Geometric decomposition for **Llama-3.1-8B** under identity alignment ($W=I$) on MMLU. Each benchmark section reports Spearman’s $r_s(\mathcal{B}, |\Delta\mathcal{R}|)$ across all quantization variants. Shading: $\Omega < 0.80$ / $\Omega < 0.95$ on $(\Omega, \delta, \mathcal{B}, |\Delta\mathcal{R}|)$; $\gamma = 0$ when the head is preserved ($H_T = H_P$).

Dataset	Family	Method	ρ_T	ρ_P	Ω	δ	γ	PRISM \mathcal{B}	$ \Delta\mathcal{R} $
MMLU ($r_s=0.91$)	GGUF	FP16	138.96	138.96	0.9998	6.4546	0	6.4546	0.0017
		Q8_0	138.96	139.18	0.9988	17.7313	5.5072	23.2386	0.0002
		Q6_K	138.96	139.83	0.9945	38.2729	17.3026	55.5755	0.0049
		Q5_K_M	138.96	139.94	0.9912	48.5266	17.3177	65.8443	0.0045
		Q4_K_M	138.96	140.36	0.9764	79.3320	17.4187	96.7506	0.0356
		Q3_K_M	138.96	140.33	0.9413	125.0579	17.3380	142.3959	0.0808
	Q2_K	138.96	143.86	0.7750	248.2226	17.8641	266.0867	0.3658	
	BnB	INT8	138.96	139.09	0.9880	56.3886	0	56.3886	0.0265
		NF4	138.96	144.16	0.9124	155.4506	0	155.4506	0.0750
		FP4	138.96	138.10	0.9196	145.1767	0	145.1767	0.1306
GPTQ	GPTQ-4bit	138.96	140.37	0.9298	136.7867	0	136.7867	0.1422	

Benchmarks and scoring. Five benchmarks: **MMLU** [28], **ARC** [29] (multiple-choice knowledge), **TriviaQA** [30], **SQuAD** [31] (short-horizon QA), and **GSM8K** [32] (multi-step reasoning). All risks are computed teacher-forced (prompt c and targets y scored in a single forward pass over the gold span), producing a deterministic per-sample CE loss whose expectation gives the model’s risk \mathcal{R}_M , and $|\Delta\mathcal{R}|$ is the target-vs-proxy gap we report.

Calibration and hyperparameters. PRISM and $|\Delta\mathcal{R}|$ are evaluated on fixed held-out subsets shared across all variants of a base (512 samples per benchmark for PTQ, 256 for LoRA forgetting); since observed $|\Delta\mathcal{R}|$ spans 1–2 orders of magnitude across variants, rankings are robust to subset choice. LoRA fine-tunes rank-32 attention adapters with frozen head (AdamW, lr 10^{-5} , batch size 16, bf16). For the regularization comparison (Sec. 5.4), both penalties operate on \mathcal{D}_{ref} (32 pre-training sequences disjoint from \mathcal{D}_{FT}): the trace-norm shape penalty sweeps $\lambda \in \{0.01, 0.05, 0.1, 0.5, 1.0\}$ and a replay-CE baseline sweeps $\lambda \in \{0.001, 0.005, 0.01, 0.05, 0.1\}$, each range matched to its penalty’s natural scale ($1-\Omega \sim 0.1$ vs. CE reference loss ~ 1 nat). Checkpoints every 25 steps, analysis at step 300; all experiments use a single NVIDIA RTX 5090 (32 GB).

5.2 Predictiveness: the bound tracks the risk gap

Quantization. The PRISM bound \mathcal{B} tracks $|\Delta\mathcal{R}|$ with strong rank correlation across Llama and Qwen (mean Spearman $r_s = 0.820 \pm 0.0471$ (SEM) over the 2×5 grid; Fig. 2; Ministral/DeepSeek replication in Appendix Fig. 5). Bit-width drives the bound monotonically: Q8/Q6 GGUF variants

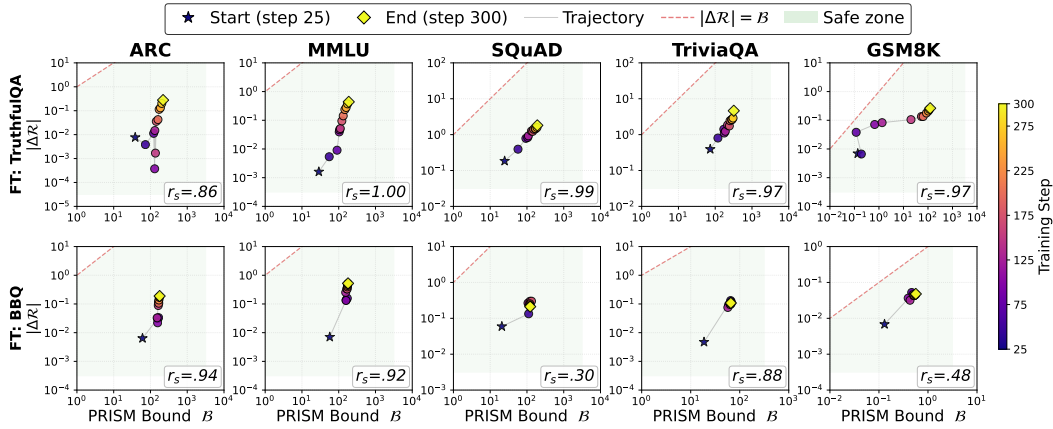


Figure 3: **Llama-3.1-8B: the PRISM bound tracks catastrophic forgetting across LoRA fine-tuning steps.** Each subplot scatters the bound \mathcal{B} (x-axis, log) against the empirical forgetting $|\Delta\mathcal{R}|$ (y-axis, log) on a downstream benchmark, with one point per LoRA checkpoint colored by training step. Rows: fine-tuning task (TruthfulQA, BBQ). Columns: downstream benchmark (ARC, MMLU, SQuAD, TriviaQA, GSM8K). Under LoRA’s frozen `lm_head`, $\gamma=0$ so \mathcal{B} reduces to backbone scale ($\Delta\rho$) and shape ($1-\Omega$) drift. Spearman r_s per subplot is annotated in each panel. Qwen3-8B replication: Appendix G.

sit in the low- \mathcal{B} /low- $|\Delta\mathcal{R}|$ corner, while Q2 configurations move into the upper-right region where shape distortion ($1-\Omega$) dominates the feature error (Table 1). All evaluated variants lie below the $y=x$ line (Fig. 2), confirming Theorem 1’s upper-bound guarantee empirically; the bit-width tier ordering ($Q8/Q6 < Q5/Q4 < Q3/Q2$ in \mathcal{B}) holds across both families.

On Llama MMLU specifically, this correlation reaches Spearman $r_s = 0.91$: as bit-width drops from Q8 to Q2, \mathcal{B} and $|\Delta\mathcal{R}|$ rise together (Table 1); the remaining Llama benchmarks (TriviaQA, ARC, SQuAD, GSM8K), the Qwen3-8B counterpart, the feature-only (δ) scatter, and Ministral/DeepSeek decompositions are in Appendices F.2–F.3.

LoRA forgetting. The same predictiveness extends to fine-tuning-induced drift (Fig. 3): as LoRA fine-tuning proceeds on TruthfulQA or BBQ from step 25 to step 300, the bound computed on *downstream* benchmarks tracks the empirical cross-entropy drift step-by-step, with mean Spearman $r_s = 0.831 \pm 0.0722$ over the 2×5 downstream cells, comparable to the PTQ grid (Fig. 2). On Llama TruthfulQA in particular, forgetting accumulates progressively across checkpoints, where \mathcal{B} and $|\Delta\mathcal{R}|$ trend together (mean $r_s = 0.958$ across the 5 downstream benchmarks). The Qwen3-8B replication (Appendix G) reproduces both patterns in most cells.

5.3 Decomposability: three axes, three failure modes

Scalar correlation alone matches prior representational similarity work in answering *whether* a variant has degraded. PRISM’s decomposition adds *which*: the dominant axis of Theorem 1 reads off directly from the per-variant numbers and maps to a distinct empirical failure mode.

Shape distortion (low-bit PTQ). At Q2 and Q3 across all four families tested (Appendix F.3 for Ministral and DeepSeek), the shape term $2\rho_T\rho_P(1-\Omega)$ typically dominates the scale term $(\Delta\rho)^2$, often by orders of magnitude. At Llama-Q2_K MMLU (Table 1), ρ_P exceeds ρ_T only modestly ($\Delta\rho \approx 4.9$, scale ≈ 24) yet Ω drops to 0.78, driving shape ($\approx 9,000$) to dominate; Ministral-Q2_K SQuAD shows the same pattern (~ 3 vs $\sim 9,000$). This is consistent with low-bit PTQ corrupting the relational structure of the feature manifold rather than its global scale—a separation invisible to any scalar similarity metric. The same shape dominance appears in LoRA forgetting: at Llama TruthfulQA-FT on TriviaQA (no-reg baseline; Table 18, Appendix), Ω drops to 0.76 with shape ($\approx 10,000$) outweighing scale (≈ 35) by $\sim 280\times$ —motivating the shape regularizer of Sec. 5.4.

Scale-axis separability. The scale axis surfaces as a non-redundant channel in two regimes. In PTQ, Qwen3-Base Q2_K on GSM8K is a scale-axis outlier: ρ_P jumps from 267 to 313 ($|\Delta\rho|=46$, vs. ≤ 8 for all other Qwen3 quantization variants on this benchmark), separately from the shape drift (Table 12, Appendix). In LoRA forgetting, the sign of $\Delta\rho$ varies with source task—TruthfulQA-FT drives $\rho_P > \rho_T$ on all five benchmarks, while BBQ-FT produces $\rho_P < \rho_T$ on ARC/MMLU

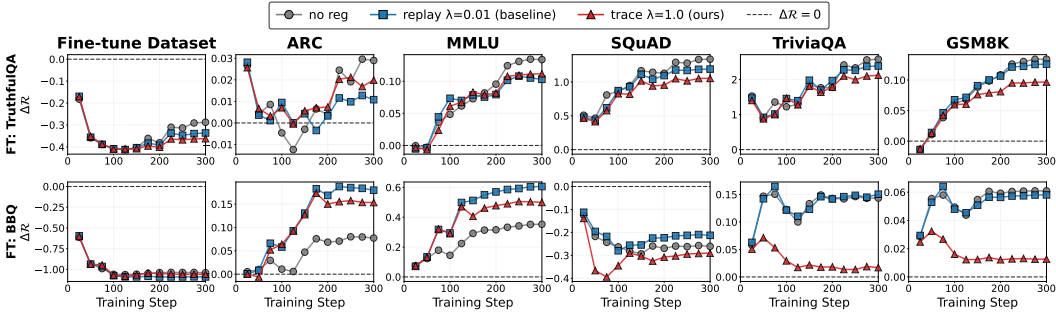


Figure 4: **Shape regularization vs. replay-CE on Llama-3.1-8B.** LoRA fine-tuning on TruthfulQA (top) and BBQ (bottom) under three configurations: *no reg* (anchor), the *replay* baseline, and *our trace* (Eq. 8); the latter two share a 32-sample reference set and are each method’s sweep $|\Delta\mathcal{R}|$ -best. Our trace cuts downstream mean $|\Delta\mathcal{R}|$ further than the replay baseline; per-benchmark Ω and $|\Delta\mathcal{R}|$ in Table 2. Qwen3-8B replication: Appendix G.

Table 2: Regularization comparison for **Llama-3.1-8B** fine-tuned on **TruthfulQA** (identity alignment $W=I$; metrics at step 300). Rows: Ω (higher = more shape preserved) and $|\Delta\mathcal{R}|$ (lower = less forgetting). **Bold / underline**: 1st / 2nd-best per benchmark group. Across-benchmark unweighted means for [no reg / replay $\lambda=0.01$ (baseline) / trace $\lambda=1.0$ (ours)]: $\Omega = 0.906 / 0.915 / \mathbf{0.931}$; $|\Delta\mathcal{R}| = 0.843 / 0.764 / \mathbf{0.681}$. In this frozen-1m_head LoRA setting $\gamma \equiv 0$ and $\rho_T \approx \rho_P$, so δ and \mathcal{B} track Ω ; the full decomposition is in Appendix Tables 18–21.

	ARC			MMLU			SQuAD			TriviaQA			GSM8K		
	no reg	replay	trace	no reg	replay	trace	no reg	replay	trace	no reg	replay	trace	no reg	replay	trace
$\Omega \uparrow$	0.916	<u>0.918</u>	0.932	0.943	<u>0.945</u>	0.954	0.923	<u>0.935</u>	0.948	0.759	<u>0.781</u>	0.821	0.991	<u>0.996</u>	1.000
$ \Delta\mathcal{R} \downarrow$	0.029	0.011	<u>0.020</u>	0.134	0.103	<u>0.112</u>	1.337	<u>1.191</u>	1.054	2.583	<u>2.388</u>	2.124	0.134	<u>0.126</u>	0.097

(Tables 18, 19, Appendix). The $(\Delta\rho, 1-\Omega)$ decomposition makes these *qualitatively different drift geometries* visible—invisible to scalar similarity.

Head divergence (GGUF k-quant tiers that quantize 1m_head). When the protocol quantizes the output embedding, the head term γ becomes the dominant arm. At Qwen3-Base Q6_K on SQuAD (Table 12, Appendix F.3), backbone scale and shape are essentially perfect ($(\Delta\rho)^2 \approx 0.12$, $\Omega \approx 1$), so $\delta=1.18$, yet the quantized output embedding alone contributes $\gamma=75.77$ —making γ essentially the entire bound (Q8_0 shows the same pattern: $\delta=0.74$, $\gamma=23.96$). Under BnB INT8 the same Qwen3-Base keeps $\gamma \equiv 0$ by construction, leaving only $\delta=3.81$ as the bound—a $20\times$ reduction from Q6_K’s $\mathcal{B}=76.95$, determined entirely by which protocol quantizes 1m_head. The decomposition makes this protocol-level switch read off directly, identifying not just the magnitude of degradation but its dominant channel.

From diagnosis to remediation. Each dominant axis suggests an axis-specific remediation. Scale collapse admits per-channel outlier smoothing [17], and head divergence admits FP16-1m_head retention. Shape preservation admits two lifecycle-specific instances: Hessian-aware reconstruction at PTQ time, and differentiable trace regularization at LoRA training time (Sec. 5.4). The bound thus turns from a scalar score into an axis-level diagnostic with actionable structure.

5.4 Actionability: from diagnostic to training objective

The decomposition of Sec. 5.3 suggests an immediate intervention: shape drift dominates LoRA forgetting, and $1-\Omega$ is differentiable in Z_t . We add the trace-norm penalty $\lambda(1-\Omega(Z_0^{\text{ref}}, Z_t^{\text{ref}}))$ on the reference set \mathcal{D}_{ref} . To isolate shape preservation from data re-fitting, we compare against a replay-CE baseline that uses the same \mathcal{D}_{ref} (cross-entropy on \mathcal{D}_{ref} , swept over λ).

Fig. 4 and Table 2 compare our trace at $\lambda=1.0$ against the replay baseline at $\lambda=0.01$ on Llama-3.1-8B (no regularization as anchor reference; both λ chosen as each method’s sweep optimum under the identical evaluation protocol). Our trace cuts mean downstream $|\Delta\mathcal{R}|$ on TruthfulQA from 0.84 (no reg) to 0.68 (−19%); the replay baseline only reaches 0.76 (−9%). On Llama BBQ, fine-tuning is less shape-disruptive (mean baseline $\Omega = 0.932$ vs. TruthfulQA’s 0.906); trace still lifts Ω (0.93 \rightarrow 0.98) while replay leaves it flat. Mechanistically, replay reduces forgetting indirectly by re-fitting reference data (without directly targeting Ω); trace contracts the shape arm of the bound at

Table 3: **Component-wise ablation: PRISM ranks variants strongly under both alignments.** Rows add bound components cumulatively (shape \rightarrow + scale \rightarrow + head); larger r_s = better ranking; **bold / underline**: 1st / 2nd-best within each block. Top block: identity $W=I$ (main text default; \mathcal{B} reaches $r_s=0.82$). Bottom block: Procrustes-optimal $W=W_N$ (\mathcal{B}_N reaches $r_s=0.91$, modestly tighter since W_N minimizes the alignment residual). The main text adopts $W=I$ for SVD-free differentiability and the $H_T=H_P$ head-term simplification in frozen-`lm_head` regimes.

Metric		Llama (5 benchmarks)	Qwen3 (5 benchmarks)	Mean r_s (10 cells)
Ω	(shape similarity; baseline)	0.825	0.783	0.804
δ	(+ scale; feature alignment error)	0.881	0.855	0.868
\mathcal{B}	(+ head; full bound, $W=I$)	<u>0.828</u>	<u>0.813</u>	<u>0.820</u>
Ω_N	(shape similarity; baseline)	0.839	0.773	0.806
δ_N	(+ scale; feature alignment error)	<u>0.898</u>	<u>0.847</u>	<u>0.873</u>
\mathcal{B}_N	(+ head; full bound, $W=W_N$)	0.927	0.896	0.912

the source. Task-dependence and the axis-guided gating signal are analyzed in Appendix H (Table 22). The Qwen3-8B replication and BBQ per-variant tables are in Appendix G.

5.5 Ablation: component-wise contributions

Table 3 measures the marginal ranking contribution of each PRISM bound component. Under $W=I$ (top block), the shape-only similarity Ω already achieves mean $r_s=0.804$: token-feature relational geometry alone carries most of the variant-ranking signal. Adding scale to form δ lifts the mean to 0.868 (+0.064)—scale collapse is the single largest per-component contributor. Adding the head term to form \mathcal{B} moves the aggregate to 0.820: $\gamma>0$ engages only on GGUF k-quant tiers that quantize `lm_head` while $\gamma\equiv 0$ on GPTQ/BnB (FP16 head), so pooling across these heterogeneous γ -regimes adds variance to the pooled rank order while preserving the bound’s validity. \mathcal{B} remains our default—it is Theorem 1’s certified upper bound and the only valid metric whenever $\gamma>0$.

Under $W=W_N$ (bottom block), $\Omega_N \rightarrow \delta_N \rightarrow \mathcal{B}_N$ all rise monotonically and \mathcal{B}_N achieves $r_s=0.912$, confirming the head term contributes most when the alignment absorbs the $H_T \rightarrow H_P$ rotation. The $W=I$ trace specialization trades ~ 0.09 Spearman for SVD-free differentiability, frozen-`lm_head` head-term simplification, and consistency with the Sec. 3.5 regularizer. Both alignments thus yield strong predictiveness; the choice between them is primarily design-driven.

6 Discussion

PRISM combines a closed-form geometric bound on $|\mathcal{R}_T - \mathcal{R}_P|$ with an exact three-axis decomposition (scale, shape, head). The decomposition turns variant comparison from a scalar similarity score into an axis-level diagnostic that pinpoints *which* part has drifted; the bound applies to PTQ and frozen-head LoRA, and the differentiable Ω doubles as a training-time regularizer. Empirically, this single framework ranks variants with comparable Spearman across both regimes ($r_s \approx 0.82$ on PTQ, 0.831 on LoRA), the three axes localize qualitatively distinct failure modes, and the axis-guided shape regularizer outperforms experience replay in aggregate at mitigating downstream forgetting.

Scope and limitations. PRISM bounds the cross-entropy risk gap to a reference base; it is calibrated for variant ranking, where Spearman correlations are strong across both PTQ and LoRA settings (Sec. 5.2). Tight absolute estimation of $|\Delta \mathcal{R}|$ is a complementary problem we leave to future work. Our evaluation uses teacher-forced features for efficiency (a single deterministic forward pass per variant, without sampling noise or decoding strategy to control for); the bound applies unchanged to any (Z_T, Z_P) matrices, including features collected along free-running generation trajectories—a direct extension we leave to future work. The shape regularizer of Sec. 5.4 handles the shape axis directly via training; per-axis protocol-level mitigations (Sec. 5.3) remain a research follow-up enabled by the diagnostic.

Future work. We describe future directions in detail in Appendix I, including **beyond LoRA forgetting** (analyze and regularize SFT/distillation drift), **diagnostic applications** (OOD detection, hyperparameter transfer, drift monitoring), and **beyond LLMs** (ViT, contrastive image encoders).

Acknowledgments

We thank Chih-Han Yu for inspiring this work, and the Appier AI Research team members for their support. This work was supported in part by the National Science and Technology Council, Taiwan, under Grants 114-2628-E-002-021- and 115-2634-F-002 -012-, and the Taiwan Centers of Excellence. Shao-Hua Sun was supported by the Yushan Fellow Program of the Ministry of Education, Taiwan.

References

- [1] Elias Frantar, Saleh Ashkboos, Torsten Hoefer, and Dan Alistarh. GPTQ: Accurate post-training quantization for generative pre-trained transformers. In *International Conference on Learning Representations (ICLR)*, 2023.
- [2] Tim Dettmers, Mike Lewis, Younes Belkada, and Luke Zettlemoyer. LLM.int8(): 8-bit Matrix Multiplication for Transformers at Scale. In S. Koyejo, S. Mohamed, A. Agarwal, D. Belgrave, K. Cho, and A. Oh, editors, *Advances in Neural Information Processing Systems*, volume 35, pages 30318–30332. Curran Associates, Inc., 2022.
- [3] Edward J Hu, Yelong Shen, Phillip Wallis, Zeyuan Allen-Zhu, Yuanzhi Li, Shean Wang, Lu Wang, and Weizhu Chen. LoRA: Low-Rank Adaptation of Large Language Models. In *International Conference on Learning Representations (ICLR)*, 2022.
- [4] Geoffrey Hinton, Oriol Vinyals, and Jeff Dean. Distilling the knowledge in a neural network. *arXiv preprint arXiv:1503.02531*, 2015.
- [5] Aaron Grattafiori, Abhimanyu Dubey, Abhinav Jauhri, Abhinav Pandey, Abhishek Kadian, Ahmad Al-Dahle, Aiesha Letman, Akhil Mathur, Alan Schelten, Amy Yang, et al. The Llama 3 herd of models. *arXiv preprint arXiv:2407.21783*, 2024.
- [6] Qwen Team. Qwen3 technical report. *arXiv preprint arXiv:2505.09388*, 2025.
- [7] Maithra Raghu, Justin Gilmer, Jason Yosinski, and Jascha Sohl-Dickstein. SVCCA: Singular vector canonical correlation analysis for deep learning dynamics and interpretability. In *Advances in Neural Information Processing Systems (NeurIPS)*, 2017.
- [8] Simon Kornblith, Mohammad Norouzi, Honglak Lee, and Geoffrey Hinton. Similarity of neural network representations revisited. In *International Conference on Machine Learning (ICML)*, 2019.
- [9] Frances Ding, Jean-Stanislas Denain, and Jacob Steinhardt. Grounding representation similarity with statistical testing. In *Advances in Neural Information Processing Systems (NeurIPS)*, 2021.
- [10] MohammadReza Davari, Stefan Horoi, Amine Natic, Guillaume Lajoie, Guy Wolf, and Eugene Belilovsky. Reliability of CKA as a similarity measure in deep learning. In *International Conference on Learning Representations (ICLR)*, 2023.
- [11] Max Klabunde, Tobias Schumacher, Markus Strohmaier, and Florian Lemmerich. Similarity of neural network models: A survey of functional and representational measures. *ACM Computing Surveys*, 57(9):1–52, 2025. doi: 10.1145/3728458.
- [12] Kiho Park, Yo Joong Choe, and Victor Veitch. The linear representation hypothesis and the geometry of large language models. In *International Conference on Machine Learning (ICML)*, 2024.
- [13] Luca Moschella, Valentino Maiorca, Marco Fumero, Antonio Norelli, Francesco Locatello, and Emanuele Rodolà. Relative representations enable zero-shot latent space communication. In *International Conference on Learning Representations (ICLR)*, 2023.
- [14] Alex H Williams, Erin Kunz, Simon Kornblith, and Scott W Linderman. Generalized shape metrics on neural representations. In *Advances in Neural Information Processing Systems (NeurIPS)*, 2021.

- [15] Sarah E Harvey, David Lipshutz, and Alex H Williams. What representational similarity measures imply about decodable information. In *Proceedings of UniReps: the Second Edition of the Workshop on Unifying Representations in Neural Models*, volume 285 of *Proceedings of Machine Learning Research*, pages 140–151. PMLR, 2024.
- [16] Minyoung Huh, Brian Cheung, Tongzhou Wang, and Phillip Isola. Position: The platonic representation hypothesis. In *Proceedings of the 41st International Conference on Machine Learning*, volume 235 of *Proceedings of Machine Learning Research*, pages 20617–20642. PMLR, 2024.
- [17] Guangxuan Xiao, Ji Lin, Mickael Seznec, Hao Wu, Julien Demouth, and Song Han. SmoothQuant: Accurate and Efficient Post-Training Quantization for Large Language Models. In *International Conference on Machine Learning (ICML)*, pages 38087–38099. PMLR, 2023.
- [18] James Kirkpatrick, Razvan Pascanu, Neil Rabinowitz, Joel Veness, Guillaume Desjardins, Andrei A Rusu, Kieran Milan, John Quan, Tiago Ramalho, Agnieszka Grabska-Barwinska, et al. Overcoming catastrophic forgetting in neural networks. *Proceedings of the National Academy of Sciences (PNAS)*, 114(13):3521–3526, 2017.
- [19] Jared Kaplan, Sam McCandlish, Tom Henighan, Tom B Brown, Benjamin Chess, Rewon Child, Scott Gray, Alec Radford, Jeffrey Wu, and Dario Amodei. Scaling laws for neural language models. *arXiv preprint arXiv:2001.08361*, 2020.
- [20] Jordan Hoffmann, Sebastian Borgeaud, Arthur Mensch, Elena Buchatskaya, Trevor Cai, Eliza Rutherford, Diego de Las Casas, Lisa Anne Hendricks, Johannes Welbl, Aidan Clark, et al. Training compute-optimal large language models. In *Advances in Neural Information Processing Systems (NeurIPS)*, 2022.
- [21] Felipe Maia Polo, Lucas Weber, Leshem Choshen, Yuekai Sun, Gongjun Xu, and Mikhail Yurochkin. tinyBenchmarks: Evaluating LLMs with fewer examples. In *International Conference on Machine Learning (ICML)*, 2024.
- [22] Yotam Perlitz, Elron Bandel, Ariel Gera, Ofir Arviv, Liat Ein-Dor, Eyal Shnarch, Noam Slonim, Michal Shmueli-Scheuer, and Leshem Choshen. Efficient benchmarking (of language models). In *Proceedings of the 2024 Conference of the North American Chapter of the Association for Computational Linguistics: Human Language Technologies (Volume 1: Long Papers)*, pages 2519–2536, Mexico City, Mexico, 2024. Association for Computational Linguistics. doi: 10.18653/v1/2024.naacl-long.139.
- [23] Collin Burns, Pavel Izmailov, Jan Hendrik Kirchner, Bowen Baker, Leo Gao, Leopold Aschenbrenner, Yining Chen, Adrien Ecoffet, Manas Joglekar, Jan Leike, Ilya Sutskever, and Jeffrey Wu. Weak-to-strong generalization: Eliciting strong capabilities with weak supervision. In *International Conference on Machine Learning (ICML)*, 2024.
- [24] Alexander H Liu et al. Ministral 3. *arXiv preprint arXiv:2601.08584*, 2026.
- [25] DeepSeek-AI. DeepSeek-R1: Incentivizing reasoning capability in LLMs via reinforcement learning. *Nature*, 645:633–638, 2025. doi: 10.1038/s41586-025-09422-z.
- [26] Stephanie Lin, Jacob Hilton, and Owain Evans. TruthfulQA: Measuring how models mimic human falsehoods. In *Proceedings of the 60th Annual Meeting of the Association for Computational Linguistics (Volume 1: Long Papers)*, pages 3214–3252, Dublin, Ireland, 2022. Association for Computational Linguistics. doi: 10.18653/v1/2022.acl-long.229.
- [27] Alicia Parrish, Angelica Chen, Nikita Nangia, Vishakh Padmakumar, Jason Phang, Jana Thompson, Phu Mon Htut, and Samuel R. Bowman. BBQ: A hand-built bias benchmark for question answering. In *Findings of the Association for Computational Linguistics: ACL 2022*, pages 2086–2105, Dublin, Ireland, 2022. Association for Computational Linguistics. doi: 10.18653/v1/2022.findings-acl.165.
- [28] Dan Hendrycks, Collin Burns, Steven Basart, Andy Zou, Mantas Mazeika, Dawn Song, and Jacob Steinhardt. Measuring massive multitask language understanding. In *International Conference on Learning Representations (ICLR)*, 2021.

- [29] Peter Clark, Isaac Cowhey, Oren Etzioni, Tushar Khot, Ashish Sabharwal, Carissa Schoenick, and Oyvind Tafjord. Think you have solved question answering? Try ARC, the AI2 reasoning challenge. *arXiv preprint arXiv:1803.05457*, 2018.
- [30] Mandar Joshi, Eunsol Choi, Daniel S. Weld, and Luke Zettlemoyer. TriviaQA: A large scale distantly supervised challenge dataset for reading comprehension. In *Proceedings of the 55th Annual Meeting of the Association for Computational Linguistics (Volume 1: Long Papers)*, pages 1601–1611, Vancouver, Canada, 2017. Association for Computational Linguistics. doi: 10.18653/v1/P17-1147.
- [31] Pranav Rajpurkar, Jian Zhang, Konstantin Lopyrev, and Percy Liang. SQuAD: 100,000+ questions for machine comprehension of text. In *Proceedings of the 2016 Conference on Empirical Methods in Natural Language Processing*, pages 2383–2392, Austin, Texas, 2016. Association for Computational Linguistics. doi: 10.18653/v1/D16-1264.
- [32] Karl Cobbe, Vineet Kosaraju, Mo Bavarian, Mark Chen, Heewoo Jun, Lukasz Kaiser, Matthias Plappert, Jerry Tworek, Jacob Hilton, Reiichiro Nakano, Christopher Hesse, and John Schulman. Training verifiers to solve math word problems. *arXiv preprint arXiv:2110.14168*, 2021.
- [33] Peter H Schönemann. A generalized solution of the orthogonal Procrustes problem. *Psychometrika*, 31(1):1–10, 1966.
- [34] John C Gower and Garnt B Dijkstra. *Procrustes Problems*. Oxford University Press, 2004.
- [35] Kawin Ethayarajh. How contextual are contextualized word representations? Comparing the geometry of BERT, ELMo, and GPT-2 embeddings. In *Proceedings of the 2019 Conference on Empirical Methods in Natural Language Processing (EMNLP)*, 2019.

Appendix

Table of Contents

A Proof of the unified risk bound (Theorem 1)	13
A.1 Relation to classical Procrustes shape metrics	14
A.2 Step 1: risk decomposition via triangle inequality	14
A.3 Step 2: bounding the feature alignment error δ	14
A.4 Step 3: exact geometric decomposition	15
A.5 Step 4: bounding the head discrepancy γ	17
A.6 Step 5: assembling the unified bound	18
B Tightness of nuclear norm over Frobenius norm	18
C Extension to general orthogonal alignments	19
C.1 The general bound for arbitrary W	19
C.2 The trace specialization ($W = I$)	19
C.3 Joint optimization on the Stiefel manifold	20
D Formal extension to autoregressive generation	20
E Model and quantization details	21
E.1 Target models	21
E.2 Quantization backends and bit-widths	21
E.3 Per-model GPTQ repositories	22
E.4 GGUF repositories	22
E.5 Backend coverage summary	22
F Quantization replication, feature-only scatter, and per-model tables	23
F.1 Replication on Ministral and DeepSeek	23
F.2 Feature-only scatter	23
F.3 Per-model decomposition tables	23
G Qwen3-8B forgetting and shape-regularization replications	31
G.1 Forgetting: bound tracks cross-task drift on Qwen3-8B	32
G.2 Shape regularization: Qwen3-8B replication	33
G.3 Additional trace-norm decomposition tables	33
H When shape regularization helps: task-dependence	33
I Future work	36

A Proof of the unified risk bound (Theorem 1)

We provide the complete proof of Theorem 1, which the main text states for general $W \in \mathcal{O}(d)$ (trace family Ω_W , Eq. 3). The proof proceeds through five self-contained steps: risk decomposition via triangle inequality, Lipschitz analysis of cross-entropy with respect to features, the alignment-residual decomposition (whose Procrustes-optimal specialization $W = W_N$ yields the nuclear form Ω_N via SVD), covariance-adjusted head bound, and final assembly. The identity-alignment specialization $W = I$ (used throughout Sec. 5 and the regularizer of Sec. 3.5) and the $W = W_N$ specialization (used in the Sec. 5.5 ablation) follow as corollaries of the same proof.

A.1 Relation to classical Procrustes shape metrics

The left-hand side of Eq. (2) at $W = W_N$ is the squared Procrustes size-and-shape distance $d_1^2(Z_T, Z_P)$ studied in the generalized shape metrics framework [14] and its recent decodability analysis [15]. Expanding d_1^2 reveals that the nuclear norm $\|Z_T^\top Z_P\|_*$ appears inside any Procrustes-based similarity; accordingly, our contribution is *not* the Procrustes distance itself. Rather, it is (a) the explicit split of this residual into the scale term $(\rho_T - \rho_P)^2$ and the shape term $2\rho_T\rho_P(1 - \Omega_N)$, which the shape-metric literature treats jointly as a single descriptive dissimilarity, and (b) its lifting to a functional-risk bound (Theorem 1). Section 4 (Quantization and LoRA Forgetting paragraphs) shows that the two arms of this split have qualitatively different practical meanings and dominate the risk gap under different LLM lifecycle settings.

A.2 Step 1: risk decomposition via triangle inequality

Setup. Recall that the risk of model M is $\mathcal{R}_M = \mathbb{E}_{(x,y)}[\ell(\phi_M(x) \cdot H_M, y)]$, where ℓ is the cross-entropy loss (Eq. 1). For any orthogonal alignment $W \in \mathcal{O}(d)$, introduce the hybrid risk:

$$\mathcal{R}_{P \rightarrow T} := \mathbb{E}_{(x,y)}[\ell(\phi_P(x) W \cdot H_T, y)]. \quad (9)$$

This evaluates the target’s head H_T on proxy features aligned by W , serving as a bridge between \mathcal{R}_T and \mathcal{R}_P . The proof below holds for any $W \in \mathcal{O}(d)$; the two specializations relevant to the paper are $W = I$ (identity alignment, trace form Ω , used throughout the main text) and $W = W_N := \arg \min_W \|Z_T - Z_P W\|_F^2$ (Procrustes-optimal, nuclear form Ω_N , Sec. 5.5 ablation).

Decomposition. By the triangle inequality on absolute values:

$$|\mathcal{R}_T - \mathcal{R}_P| \leq \underbrace{|\mathcal{R}_T - \mathcal{R}_{P \rightarrow T}|}_{\text{Feature Alignment Error } \delta} + \underbrace{|\mathcal{R}_{P \rightarrow T} - \mathcal{R}_P|}_{\text{Head Discrepancy } \gamma}. \quad (10)$$

δ measures how features differ through the same head H_T ; γ measures how heads differ on the same aligned features.

A.3 Step 2: bounding the feature alignment error δ

Lipschitz property of cross-entropy with respect to features. We bound δ by showing that the cross-entropy loss is Lipschitz continuous in the feature vector z . Define the end-to-end composition $g_T(z, y) := \ell(z \cdot H_T, y)$, treating the classification head H_T and the cross-entropy loss as a single map from features to scalar loss. We bound g_T via direct gradient analysis rather than the Lipschitz composition rule (loss-Lipschitz $\sqrt{2}$ times head operator norm $\|H_T\|_2$): the composition rule is agnostic to the softmax output and gives the spectral constant $\sqrt{2}\|H_T\|_2$ (Remark below), whereas the gradient $\nabla_z g_T = H_T(\hat{p} - e_y)$ exposes the predicted distribution \hat{p} and lets us derive a constant set by pairwise token-embedding distances instead. Our goal is to find the tightest constant K_{feat} such that:

$$|g_T(z_1, y) - g_T(z_2, y)| \leq K_{\text{feat}} \|z_1 - z_2\|_2, \quad \forall z_1, z_2, y. \quad (11)$$

Computing the gradient. The logit vector is $v = z \cdot H_T \in \mathbb{R}^V$, and the cross-entropy loss is $\ell(v, y) = -v_y + \log \sum_{j=1}^V e^{v_j}$. The gradient with respect to the logits is:

$$\frac{\partial \ell}{\partial v} = \hat{p} - e_y, \quad (12)$$

where $\hat{p} = \text{softmax}(v) \in \mathbb{R}^V$ and e_y is the one-hot vector at index y . Applying the chain rule to obtain the gradient with respect to features:

$$\nabla_z \ell = H_T(\hat{p} - e_y) = \sum_{j=1}^V (\hat{p}_j - \delta_{jy}) h_{T,j}, \quad (13)$$

where $h_{T,j}$ denotes the j -th column of H_T (the embedding vector for token j).

Simplex polarization. We now derive a tight bound on $\|\nabla_z \ell\|_2$ by exploiting the probability simplex constraint $\sum_j \hat{p}_j = 1$. Expanding the gradient for true class y :

$$\nabla_z \ell = (\hat{p}_y - 1) h_{T,y} + \sum_{j \neq y} \hat{p}_j h_{T,j}. \quad (14)$$

Since $1 - \hat{p}_y = \sum_{j \neq y} \hat{p}_j$, we can rewrite:

$$\nabla_z \ell = -\left(\sum_{j \neq y} \hat{p}_j\right) h_{T,y} + \sum_{j \neq y} \hat{p}_j h_{T,j} = \sum_{j \neq y} \hat{p}_j (h_{T,j} - h_{T,y}). \quad (15)$$

This reveals that the gradient is a *non-negative linear combination* of pairwise differences between incorrect-class embeddings and the correct-class embedding, with weights \hat{p}_j summing to $1 - \hat{p}_y \leq 1$. Taking the norm:

$$\|\nabla_z \ell\|_2 \leq \sum_{j \neq y} \hat{p}_j \|h_{T,j} - h_{T,y}\|_2 \leq \max_{j \neq y} \|h_{T,j} - h_{T,y}\|_2 \cdot \underbrace{\sum_{j \neq y} \hat{p}_j}_{\leq 1}. \quad (16)$$

The bound depends on the true class y only through $\max_{j \neq y} \|h_{T,j} - h_{T,y}\|_2$. Taking the supremum over $y \in \{1, \dots, V\}$ extends the maximum to all ordered pairs (j, y) with $j \neq y$ (and the $j = y$ case contributes 0), giving the full pairwise diameter:

$$K_{\text{feat}} = \max_{j,k} \|h_{T,j} - h_{T,k}\|_2. \quad (17)$$

Remark. This bound depends on the *relative distances* between token embeddings, not their absolute magnitudes. A uniform shift $H_T \rightarrow H_T + c\mathbf{1}^\top$ does not change K_{feat} . A naive Cauchy–Schwarz bound gives $K_{\text{feat}}^{\text{naive}} = \sqrt{2}\|H_T\|_2$, which is substantially looser. Since the decomposition of Eq. (10) routes through $\mathcal{R}_{P \rightarrow T}$ (which uses H_T), K_{feat} is determined by H_T alone; it takes a single value across all proxy variants of a fixed target model and enters as a constant scaling on the feature term, not as a proxy-dependent quantity that could perturb variant ranking.

From gradient bound to Lipschitz inequality. Since $g_T(\cdot, y)$ is continuously differentiable, the gradient bound $\|\nabla_z g_T(z, y)\|_2 \leq K_{\text{feat}}$ implies the Lipschitz inequality stated above by the mean value theorem: for any z_1, z_2 ,

$$g_T(z_2, y) - g_T(z_1, y) = \int_0^1 \nabla_z g_T(z_1 + t(z_2 - z_1), y)^\top (z_2 - z_1) dt,$$

and Cauchy–Schwarz gives $|g_T(z_2, y) - g_T(z_1, y)| \leq K_{\text{feat}} \|z_2 - z_1\|_2$.

Applying the Lipschitz bound. Using the Lipschitz property with $z_1 = \phi_T(x)$ and $z_2 = \phi_P(x)W$:

$$\begin{aligned} \delta &= |\mathcal{R}_T - \mathcal{R}_{P \rightarrow T}| = \left| \mathbb{E}[g_T(\phi_T(x), y) - g_T(\phi_P(x)W, y)] \right| \\ &\leq \mathbb{E} \left[|g_T(\phi_T(x), y) - g_T(\phi_P(x)W, y)| \right] \\ &\leq K_{\text{feat}} \cdot \mathbb{E}_x [\|\phi_T(x) - \phi_P(x)W\|_2]. \end{aligned} \quad (18)$$

Applying Jensen’s inequality ($\mathbb{E}[\|X\|] \leq \sqrt{\mathbb{E}[\|X\|^2]}$) to connect this to the alignment residual:

$$\delta \leq K_{\text{feat}} \cdot \sqrt{\mathbb{E}_x [\|\phi_T(x) - \phi_P(x)W\|_2^2]} = K_{\text{feat}} \cdot \sqrt{\frac{1}{n} \|Z_T - Z_P W\|_F^2}. \quad (19)$$

Empirical values. Table 4 reports K_{feat} for all 8B models studied here, ranging from 0.93 (Mistral family) to 3.46 (Qwen3-Base); $K_{\text{pred}} = \sqrt{2}$ holds universally. These values are bounded by pairwise token-embedding distances and remain independent of V (Llama $V=128,256$, Qwen3 $V=151,936$), in contrast to the naive bound $\sqrt{2}\|H_T\|_2$ whose spectral norm grows with vocabulary size.

A.4 Step 3: exact geometric decomposition

We derive the exact identity linking the alignment residual to scale and shape mismatches. The identity holds for every $W \in \mathcal{O}(d)$; we then specialize to the two cases relevant to this paper.

Table 4: Empirical Lipschitz constants of the PRISM bound (Theorem 1) for each evaluated model. $K_{\text{pred}} = \sqrt{2}$ holds universally (Appendix A.5, simplex polarization), independent of model. K_{feat} is empirical per model, depending on the spread of token embeddings in H_T ; for the 8B-scale models studied here, K_{feat} ranges from ≈ 0.93 (Mistral family) to ≈ 3.46 (Qwen3-Base). Since K_{feat} is a constant per model, it scales the bound’s magnitude but does not affect the within-model rank correlation that PRISM is calibrated to.

Model	K_{feat}	K_{pred}
Llama-3.1-8B	2.61	$\sqrt{2}$
Ministral-3-8B	0.98	$\sqrt{2}$
Qwen3-8B	3.46	$\sqrt{2}$
DeepSeek-R1-8B	2.60	$\sqrt{2}$
Llama-3.1-8B-Instruct	2.60	$\sqrt{2}$
Ministral-3-8B-Instruct	0.93	$\sqrt{2}$
Qwen3-8B-Instruct	3.41	$\sqrt{2}$

General identity. For any $W \in \mathcal{O}(d)$, expand the squared Frobenius norm:

$$\begin{aligned} \|Z_T - Z_P W\|_F^2 &= \text{Tr}[(Z_T - Z_P W)^\top (Z_T - Z_P W)] \\ &= \|Z_T\|_F^2 + \|Z_P W\|_F^2 - 2 \text{Tr}(Z_T^\top Z_P W). \end{aligned} \quad (20)$$

Since W is orthogonal, $\|Z_P W\|_F^2 = \text{Tr}(W^\top Z_P^\top Z_P W) = \text{Tr}(Z_P^\top Z_P) = \|Z_P\|_F^2$ (cyclic trace + $W^\top W = I_d$). Therefore:

$$\|Z_T - Z_P W\|_F^2 = \|Z_T\|_F^2 + \|Z_P\|_F^2 - 2 \text{Tr}(Z_T^\top Z_P W). \quad (21)$$

Recall $\rho_M = \|Z_M\|_F / \sqrt{n}$ (so $\|Z_M\|_F^2 / n = \rho_M^2$) and $\Omega_W := \text{Tr}(Z_T^\top Z_P W) / (\|Z_T\|_F \|Z_P\|_F)$ (main-text Eq. 3). Dividing Eq. (21) by n :

$$\frac{1}{n} \|Z_T - Z_P W\|_F^2 = \rho_T^2 + \rho_P^2 - 2\rho_T \rho_P \Omega_W. \quad (22)$$

Adding and subtracting $2\rho_T \rho_P$ completes the square:

$$\frac{1}{n} \|Z_T - Z_P W\|_F^2 = \underbrace{(\rho_T - \rho_P)^2}_{\text{Scale Mismatch}} + \underbrace{2\rho_T \rho_P (1 - \Omega_W)}_{\text{Shape Mismatch}}. \quad (23)$$

This is Proposition 1 in its general form. \square

Specialization 1: $W = I$ (identity alignment, main text). Setting $W = I$ gives the trace form $\Omega \equiv \Omega_{W=I} = \text{Tr}(Z_T^\top Z_P) / (\|Z_T\|_F \|Z_P\|_F)$, and Eq. (23) becomes

$$\frac{1}{n} \|Z_T - Z_P\|_F^2 = (\rho_T - \rho_P)^2 + 2\rho_T \rho_P (1 - \Omega), \quad (24)$$

which is the form used throughout the main-text experiments and the regularizer of Sec. 3.5.

Specialization 2: $W = W_N$ (Procrustes-optimal, ablation). The alignment that minimizes the residual is the classical orthogonal Procrustes problem [33, 34]:

$$W_N := \arg \min_{W \in \mathcal{O}(d)} \|Z_T - Z_P W\|_F^2 = \arg \max_{W \in \mathcal{O}(d)} \text{Tr}(Z_T^\top Z_P W), \quad (25)$$

where the second equality follows from Eq. (21) since the first two terms are W -independent. Its closed-form SVD solution is well known; we restate it here for completeness. Let $Z_T^\top Z_P = U \Sigma V^\top$ be the SVD with $U, V \in \mathcal{O}(d)$ and $\Sigma = \text{diag}(\sigma_1, \dots, \sigma_d)$, $\sigma_i \geq 0$. By cyclic trace:

$$\text{Tr}(Z_T^\top Z_P W) = \text{Tr}(\Sigma V^\top W U) = \text{Tr}(\Sigma R), \quad R := V^\top W U \in \mathcal{O}(d). \quad (26)$$

Since $\sigma_i \geq 0$ and $|R_{ii}| \leq 1$ for any orthogonal R , $\text{Tr}(\Sigma R) = \sum_i \sigma_i R_{ii}$ is maximized at $R = I_d$, giving:

$$W_N = V U^\top, \quad \max_W \text{Tr}(Z_T^\top Z_P W) = \sum_i \sigma_i = \|Z_T^\top Z_P\|_*. \quad (27)$$

Therefore $\Omega_{W_N} = \Omega_N := \|Z_T^\top Z_P\|_* / (\|Z_T\|_F \|Z_P\|_F)$ (nuclear form, Appendix B Eq. 37), and Eq. (23) at $W = W_N$ becomes

$$\min_{W \in \mathcal{O}(d)} \frac{1}{n} \|Z_T - Z_P W\|_F^2 = (\rho_T - \rho_P)^2 + 2\rho_T \rho_P (1 - \Omega_N), \quad (28)$$

the form underlying the Sec. 5.5 ablation.

Remark 1 (W_N is the feature-side optimum, not the joint optimum). *The Procrustes alignment W_N minimizes only the feature alignment residual $\delta(W)$, not the full bound $\delta(W) + \gamma(W)$, since the head term also depends on W via $WH_T - H_P$. Appendix C.3 treats the joint optimization in full and identifies the operative alignment for each setting studied here.*

Assembling the feature bound. Combining Eq. (19) with the general decomposition Eq. (23):

$$\delta \leq K_{\text{feat}} \sqrt{(\rho_T - \rho_P)^2 + 2\rho_T \rho_P (1 - \Omega_W)}. \quad (29)$$

At $W = I$, replace Ω_W with Ω ; at $W = W_N$, with Ω_N .

A.5 Step 4: bounding the head discrepancy γ

Lipschitz property with respect to logits. The head discrepancy measures how much predictions differ when two different “effective heads” (WH_T vs. H_P) operate on the same proxy features. Let $z = \phi_P(x)$ denote the (unaligned) proxy feature. Then:

$$\gamma = |\mathcal{R}_{P \rightarrow T} - \mathcal{R}_P| = \left| \mathbb{E}[\ell(z \cdot WH_T, y) - \ell(z \cdot H_P, y)] \right|. \quad (30)$$

To bound this, we use the Lipschitz property of cross-entropy with respect to *logits*. The gradient of ℓ with respect to v is $\nabla_v \ell = \hat{p} - e_y$, with norm:

$$\|\nabla_v \ell\|_2 = \|\hat{p} - e_y\|_2. \quad (31)$$

Since \hat{p} lies on the probability simplex, $\|\hat{p}\|_2 \leq \|\hat{p}\|_1 = 1$, hence

$$\|\hat{p} - e_y\|_2^2 = \|\hat{p}\|_2^2 - 2\hat{p}_y + 1 \leq 1 - 2\hat{p}_y + 1 = 2(1 - \hat{p}_y) \leq 2.$$

The supremum $\sqrt{2}$ is approached as the model’s predicted distribution concentrates on an incorrect class ($\hat{p}_y \rightarrow 0$). Thus $K_{\text{pred}} \leq \sqrt{2}$, yielding the Lipschitz inequality $|\ell(v_1, y) - \ell(v_2, y)| \leq K_{\text{pred}} \|v_1 - v_2\|_2$ on logits.

Deriving the covariance projection. Define the head misalignment matrix $\Delta H := WH_T - H_P \in \mathbb{R}^{d \times V}$. The logit difference for a single sample is $z \cdot \Delta H = \phi_P(x)(WH_T - H_P)$, and:

$$\begin{aligned} \gamma &\leq \mathbb{E}[|\ell(z \cdot WH_T, y) - \ell(z \cdot H_P, y)|] \\ &\leq K_{\text{pred}} \cdot \mathbb{E}_z[\|z \cdot \Delta H\|_2]. \end{aligned} \quad (32)$$

Applying Jensen’s inequality on the concave square root:

$$(\mathbb{E}[\|z \cdot \Delta H\|_2])^2 \leq \mathbb{E}[\|z \cdot \Delta H\|_2^2]. \quad (33)$$

Expanding the squared norm using the trace operator:

$$\begin{aligned} \mathbb{E}[\|z \cdot \Delta H\|_2^2] &= \mathbb{E}[\text{Tr}(\Delta H^\top z^\top z \Delta H)] \\ &= \text{Tr}(\Delta H^\top \underbrace{\mathbb{E}[z^\top z]}_{\Sigma_P} \Delta H) \\ &= \|\Sigma_P^{1/2} \Delta H\|_F^2. \end{aligned} \quad (34)$$

Taking the square root:

$$\gamma \leq K_{\text{pred}} \cdot \|\Sigma_P^{1/2} (WH_T - H_P)\|_F. \quad (35)$$

Interpretation. The covariance weighting $\Sigma_P^{1/2}$ projects the head error onto the *active subspace* of the data. If the heads disagree only in directions orthogonal to the feature distribution (the null space of Σ_P), this disagreement has zero cost—it does not affect any prediction. This is sharper than the loose spectral bound $\gamma \leq K_{\text{pred}} \|WH_T - H_P\|_2 \cdot \mathbb{E}[\|z\|_2]$, which conservatively assumes worst-case alignment between features and head error. The covariance weighting $\Sigma_P^{1/2}$ instead aligns the bound with the data-active directions: head misalignment in directions the features rarely traverse contributes little, and disagreement on $\text{null}(\Sigma_P)$ contributes nothing.

A.6 Step 5: assembling the unified bound

For any $W \in \mathcal{O}(d)$, combining the risk decomposition (Eq. 10), the feature bound (Eq. 29), and the head bound (Eq. 35):

$$|\mathcal{R}_T - \mathcal{R}_P| \leq \delta + \gamma \leq K_{\text{feat}} \sqrt{(\rho_T - \rho_P)^2 + 2\rho_T\rho_P(1 - \Omega_W)} + K_{\text{pred}} \cdot \|\Sigma_P^{1/2}(WH_T - H_P)\|_F. \quad (36)$$

This is Theorem 1 in its general form. The two specializations used in the paper:

- $W = I$ (**identity alignment, main text**): $\Omega_W = \Omega$ (trace form) and $WH_T - H_P = H_T - H_P$, giving the bound used throughout Sec. 5 and the regularizer of Sec. 3.5.
- $W = W_N$ (**Procrustes-optimal, ablation**): $\Omega_W = \Omega_N$ (nuclear form, achieves the tightest feature-side specialization), giving the bound underlying the Sec. 5.5 ablation.

This completes the proof of Theorem 1. \square

B Tightness of nuclear norm over Frobenius norm

We define the nuclear-form and Frobenius-form Procrustes similarities, show that the former yields a strictly tighter alignment residual than the latter, and clarify the relationship to CKA.

Definitions. The *nuclear-form* Procrustes similarity is

$$\Omega_N(Z_T, Z_P) := \frac{\|Z_T^\top Z_P\|_*}{\|Z_T\|_F \|Z_P\|_F} = \max_{W \in \mathcal{O}(d)} \frac{\text{Tr}(Z_T^\top Z_P W)}{\|Z_T\|_F \|Z_P\|_F}, \quad (37)$$

the maximum of the trace family Ω_W (Sec. 3.2) over orthogonal alignments, attained at the Procrustes-optimal W_N (Appendix A). The *Frobenius-form* similarity is $\Omega_F := \|Z_T^\top Z_P\|_F / (\|Z_T\|_F \|Z_P\|_F)$; unlike Ω_W , it does not arise from the alignment residual at any W and is treated here as an external comparison object connecting to CKA.

Statement. For any feature matrices Z_T, Z_P :

$$\Omega_F \leq \Omega_N, \quad (38)$$

with equality if and only if the cross-moment matrix $Z_T^\top Z_P$ has at most one nonzero singular value (i.e., $\text{rank} \leq 1$).

Proof. Let $\sigma_1, \dots, \sigma_d$ be the singular values of $Z_T^\top Z_P$. Then:

$$\|Z_T^\top Z_P\|_F = \sqrt{\sum_i \sigma_i^2}, \quad \|Z_T^\top Z_P\|_* = \sum_i \sigma_i. \quad (39)$$

Since $\sigma_i \geq 0$, the basic inequality $\sum_i \sigma_i^2 \leq (\sum_i \sigma_i)^2$ (cross-terms are non-negative) gives

$$\|Z_T^\top Z_P\|_F = \sqrt{\sum_i \sigma_i^2} \leq \sum_i \sigma_i = \|Z_T^\top Z_P\|_*, \quad (40)$$

i.e., $\|\mathbf{x}\|_2 \leq \|\mathbf{x}\|_1$ for any non-negative vector. Dividing both sides by $\|Z_T\|_F \|Z_P\|_F$ gives $\Omega_F \leq \Omega_N$.

Consequence for risk bounding. Ω_F does not arise from the alignment residual $\|Z_T - Z_P W\|_F^2$ at any $W \in \mathcal{O}(d)$ (which produces only trace-based similarities Ω_W); we treat it as an external comparison object. Substituting Ω_F into the bound formula in place of Ω_W yields

$$(\rho_T - \rho_P)^2 + 2\rho_T\rho_P(1 - \Omega_F) \geq (\rho_T - \rho_P)^2 + 2\rho_T\rho_P(1 - \Omega_N), \quad (41)$$

i.e., a *strictly looser* value than the alignment-derived nuclear-form term. Among the alignment-derived members $\{\Omega_W\}$, the nuclear form Ω_N is the tightest because it exactly solves $\max_{W \in \mathcal{O}(d)} \text{Tr}(Z_T^\top Z_P W)$; the trace form Ω used in the main text (Eq. 3) satisfies $\Omega \leq \Omega_N$ in general, with equality on $Z_T^\top Z_P$ symmetric PSD (Appendix C.2).

Relation to CKA. Linear CKA [8] is defined as $\text{CKA}(Z_T, Z_P) = \|Z_T^\top Z_P\|_F^2 / (\|Z_T^\top Z_T\|_F \cdot \|Z_P^\top Z_P\|_F)$, which differs from $\Omega_F^2 = \|Z_T^\top Z_P\|_F^2 / (\|Z_T\|_F^2 \|Z_P\|_F^2)$ in its denominator. The two denominators are related by the inequality $\|Z_M^\top Z_M\|_F \leq \|Z_M\|_F^2 = \text{Tr}(Z_M^\top Z_M)$ (since $\|A\|_F \leq \text{Tr}(A)$ for any positive semidefinite A , by $\|\mathbf{x}\|_2 \leq \|\mathbf{x}\|_1$ on the non-negative eigenvalues), which gives $\text{CKA} \geq \Omega_F^2$. Hence CKA can overestimate alignment relative to Ω_F , and it is not directly substitutable into our Procrustes residual. More fundamentally, CKA is not derived from any alignment optimization and therefore lacks the alignment-grounded meaning of Ω_N , which exactly solves the Orthogonal Procrustes problem.

C Extension to general orthogonal alignments

The main text (Theorem 1) states the bound at the identity alignment $W = I$. Here we lift Theorem 1 to arbitrary orthogonal W , characterize the $W = I$ trace and $W = W_N$ nuclear specializations (the latter used in the Sec. 5.5 ablation), and treat the joint optimization over feature and head terms. The two specializations encode different priorities: W_N minimizes the feature alignment residual but generally inflates the head term, while $W = I$ keeps the head term at its minimum (vanishing exactly under frozen `lm_head`) and is SVD-free differentiable, properties that the LLM settings studied here—PTQ with FP16 head and frozen-head LoRA—require.

C.1 The general bound for arbitrary W

The exact decomposition derived in Appendix A.4 (Eq. 23) holds for every $W \in \mathcal{O}(d)$ via the alignment-dependent similarity Ω_W of Eq. 3, yielding a family of risk bounds parameterized by W :

$$|\mathcal{R}_T - \mathcal{R}_P| \leq \underbrace{K_{\text{feat}} \sqrt{(\rho_T - \rho_P)^2 + 2\rho_T\rho_P(1 - \Omega_W)}}_{\delta(W)} + \underbrace{K_{\text{pred}} \|\Sigma_P^{1/2}(WH_T - H_P)\|_F}_{\gamma(W)}. \quad (42)$$

The Procrustes solution W_N minimizes $\delta(W)$ alone, yielding $\Omega_{W_N} = \Omega_N$ (the nuclear-norm similarity, Eq. 37). However, W_N enters the head term $\gamma(W_N)$, which can be inflated when the rotation is applied to a nearly preserved head ($H_T \approx H_P$). This creates a fundamental trade-off: W_N gives the tightest feature bound but may worsen the head bound, while $W = I$ preserves head coherence at the cost of a slightly looser feature bound.

C.2 The trace specialization ($W = I$)

Setting $W = I$ recovers the main-text trace similarity $\Omega = \Omega_{W=I}$ (Eq. 3). Two structural properties characterize this specialization.

Ordering of similarities. Since the Procrustes solution maximizes $\text{Tr}(Z_T^\top Z_P W)$ over $\mathcal{O}(d)$:

$$\text{Tr}(Z_T^\top Z_P) \leq \|Z_T^\top Z_P\|_*, \quad (43)$$

which gives $\Omega \leq \Omega_N$. Equality holds if and only if $W_N = I$, i.e., $Z_T^\top Z_P$ is symmetric positive semidefinite.

When does $\Omega = \Omega_N$? Let $Z_T^\top Z_P = U\Sigma V^\top$ be the SVD. Then $\Omega = \Omega_N$ iff $VU^\top = I$, i.e., $U = V$, which holds when $Z_T^\top Z_P$ is symmetric positive semidefinite (SPSD). In post-training quantization with mild noise, $Z_T^\top Z_P \approx Z_T^\top Z_T$ is approximately SPSP, so $\Omega \approx \Omega_N$. As quantization becomes more aggressive, asymmetric perturbations cause Ω to fall below Ω_N , and this gap reflects genuine asymmetric distortion that a rotation-invariant metric would mask.

Head-side simplification. At $W = I$, the head term $K_{\text{pred}} \|\Sigma_P^{1/2}(H_T - H_P)\|_F$ carries no rotational contamination and vanishes whenever the prediction head is preserved (FP16 head under PTQ, frozen head under LoRA), recovering the regimes used throughout Sec. 5 and the regularizer of Sec. 3.5.

C.3 Joint optimization on the Stiefel manifold

The tightest bound over all orthogonal alignments requires solving:

$$W_{\text{opt}} = \arg \min_{W \in \mathcal{O}(d)} \left[\underbrace{K_{\text{feat}} \sqrt{\frac{1}{n}} \|Z_T - Z_P W\|_F^2}_{\delta(W)} + \underbrace{K_{\text{pred}} \|\Sigma_P^{1/2}(W H_T - H_P)\|_F}_{\gamma(W)} \right]. \quad (44)$$

Unlike the standard Procrustes problem (which minimizes δ alone and admits the closed-form $W_N = VU^\top$), the addition of $\gamma(W)$ introduces a quadratic dependence on W through the head term, related to the *Weighted Orthogonal Procrustes Problem* (WOPP) [34].

Why no closed-form solution exists. The feature term $\delta(W)$ is concave in $\text{Tr}(Z_T^\top Z_P W)$, while $\gamma(W)$ is convex in W . Their sum is neither convex nor concave on $\mathcal{O}(d)$, precluding a simple variational characterization.

Special case: isotropic features. If $\Sigma_P \approx \lambda I$, the head term simplifies to $K_{\text{pred}} \sqrt{\lambda} \|W H_T - H_P\|_F$, which still depends on W through the cross-term $\text{Tr}(H_P^\top W H_T)$ when $\|W H_T - H_P\|_F^2$ is expanded. The joint objective then minimizes $K_{\text{feat}} \sqrt{\|Z_T - Z_P W\|_F^2/n} + K_{\text{pred}} \sqrt{\lambda} \|W H_T - H_P\|_F$, and each term individually admits a closed-form Procrustes minimizer; the sum does not. The isotropic assumption is, in any case, unrealistic for LLM representations, which exhibit well-documented anisotropy [35].

Numerical solution. For the general case, W_{opt} can be approximated via Riemannian gradient descent on the Stiefel manifold, but this entangles scale, shape, and head components, destroying the clean physical interpretation.

Practical irrelevance for this paper’s regimes. In the two primary settings:

- **Quantization (GPTQ/BnB: $H_T = H_P$; GGUF: $H_T \approx H_P$):** The Procrustes-optimal W_N minimizes the feature term $\delta(W)$ alone but inflates the head term $\gamma(W)$ when the head is approximately preserved (cf. Appendix C.1 trade-off). We adopt $W = I$ in main analyses, where γ vanishes for FP16-head retention.
- **LoRA ($H_T = H_P$):** The head term becomes $K_{\text{pred}} \|\Sigma_P^{1/2}(W - I)H_T\|_F$, which vanishes at $W = I$ (and is generically positive at $W \neq I$). We adopt $W = I$ throughout the LoRA experiments and the shape regularizer of Sec. 3.5 as it yields the cleanest decomposition: under the frozen LoRA head ($H_T = H_P$) the choice $W = I$ gives $\Sigma_P^{1/2}(I H_T - H_P) = 0$, so $\gamma = 0$; the scale arm $(\rho_T - \rho_P)^2$ is W -invariant (observed but not actively regularized, since LoRA primarily perturbs shape rather than scale; Sec. 5.3); and the shape arm $1 - \Omega$ becomes the single differentiable training-time target. The Procrustes-optimal $W_N \neq I$ would tighten the shape arm marginally ($\Omega_N \geq \Omega$) at the cost of inflating γ and breaking the at-source shape contraction the regularizer relies on.

The Riemannian formulation becomes relevant only when comparing models with *both* rotated features and divergent heads (e.g., full-parameter SFT). We leave this setting to future work.

D Formal extension to autoregressive generation

The bound of Theorem 1 applies to any matrix pair $(Z_T, Z_P) \in \mathbb{R}^{n \times d}$ of feature vectors, whatever the origin of the rows. We spell out here the autoregressive instantiation informally summarized in Sec. 3.4.

From tokens to matrices. Fix a single sequence $(c, y_1, \dots, y_{|y|})$. Each position τ supplies a (context, target-token) pair instantiating Eq. (1) with feature $\phi_M(c, y_{<\tau}) \in \mathbb{R}^d$ and loss $\ell(\phi_M(c, y_{<\tau})H_M, y_\tau)$. Stacking the $|y|$ feature vectors into a $|y| \times d$ block recovers exactly the per-row setting that Theorem 1 controls.

Corollary 1 (Autoregressive Risk Bound). *For a single sequence $(c, y_1, \dots, y_{|y|})$, let $Z_T^{\text{AR}}, Z_P^{\text{AR}} \in \mathbb{R}^{|y| \times d}$ be the feature matrices stacked as above, with RMS scales $\rho_T^{\text{AR}}, \rho_P^{\text{AR}}$, Procrustes similarity Ω^{AR} , and covariance Σ_P^{AR} . Then*

$$|\mathcal{R}_T^{\text{AR}} - \mathcal{R}_P^{\text{AR}}| \leq K_{\text{feat}} \sqrt{(\rho_T^{\text{AR}} - \rho_P^{\text{AR}})^2 + 2\rho_T^{\text{AR}} \rho_P^{\text{AR}}(1 - \Omega^{\text{AR}})} + K_{\text{pred}} \|(\Sigma_P^{\text{AR}})^{1/2}(H_T - H_P)\|_F. \quad (45)$$

Proof. Each row of Z_M^{AR} is a feature vector of dimension d , and the Lipschitz analysis of Appendix A.3 together with the Procrustes decomposition of Appendix A.4 depend only on the matrix shape, not on the provenance of its rows. Applying Theorem 1 to $(Z_T^{\text{AR}}, Z_P^{\text{AR}})$ yields the stated inequality. \square

This unification enables one bound to cover point-wise classification (MMLU, ARC, where $|y|=1$), short-horizon QA (SQuAD, TriviaQA, where y is a 1–5 token span), and multi-step reasoning (GSM8K, where y is a chain-of-thought solution).

E Model and quantization details

E.1 Target models

Table 5 lists all target (full-precision) models evaluated in the quantization experiments. All targets are loaded in BF16 as the reference precision; an FP16 proxy is additionally included for each model to measure the BF16→FP16 precision-drift baseline.

Table 5: Target models used in quantization experiments. All models are loaded in BF16.

#	Family	HuggingFace ID	Variant	Params	d	$ V $
1	Qwen 3	Qwen/Qwen3-8B-Base	Base	8B	4096	151K
2	Llama 3.1	meta-llama/Meta-Llama-3.1-8B	Base	8B	4096	128K
3	Ministral 3	mistralai/Ministral-3-8B-Base-2512	Base	8B	4096	131K
4	Qwen 3	Qwen/Qwen3-8B	Instruct	8B	4096	151K
5	Llama 3.1	meta-llama/Meta-Llama-3.1-8B-Instruct	Instruct	8B	4096	128K
6	Ministral 3	mistralai/Ministral-3-8B-Instruct-2512	Instruct	8B	4096	131K
7	DeepSeek R1	deepseek-ai/DeepSeek-R1-Distill-Llama-8B	Distilled	8B	4096	128K

Models 2, 5 (meta-llama) are gated and require accepting the Meta Community License on HuggingFace before access.

E.2 Quantization backends and bit-widths

Every target model is evaluated against up to four quantization backends. Table 6 summarises the shared GGUF and BitsAndBytes (BnB) configurations applied uniformly across all models.

Table 6: Shared quantization tiers applied to all target models. GGUF quants use the llama.cpp k-quant scheme; BnB quants use on-the-fly quantization from the full-precision checkpoint.

Tier	Backend	Tag	Description
FP16 reference	dtype	dtype:float16	BF16→FP16 precision drift baseline
8-bit	GGUF	Q8_0	Round-to-nearest, 8-bit
	BnB	bnb:int8	LLM.int8() absmax
6-bit	GGUF	Q6_K	k-quant, 6-bit (super-blocks)
5-bit	GGUF	Q5_K_M	k-quant, 5-bit (medium)
4-bit	GGUF	Q4_K_M	k-quant, 4-bit (medium)
	BnB	bnb:nf4	NormalFloat4 (QLoRA format)
3-bit	BnB	bnb:fp4	FP4 with FP16 compute
	GGUF	Q3_K_M	k-quant, 3-bit (medium)
2-bit	GGUF	Q2_K	k-quant, 2-bit

E.3 Per-model GPTQ repositories

Table 7 lists the pre-quantized GPTQ checkpoint used for each target model. All repositories are publicly hosted on HuggingFace and loaded via the standard transformers API unless otherwise noted.

Table 7: Pre-quantized GPTQ checkpoints per model. One repository per model, corresponding to the variant actually loaded in our experiments; “—” indicates no GPTQ checkpoint was evaluated for that model. GPTQ bit-width is 4-bit (the canonical setting reported in Sec. 5.1) for all models except Qwen3-8B-Instruct, where the only public checkpoint we could load uses 8-bit.

#	Model	GPTQ Repository
1	Qwen3-8B-Base	—
2	Llama-3.1-8B	ModelCloud/Meta-Llama-3.1-8B-gptq-4bit
3	Ministral-3-Base	—
4	Qwen3-8B	JunHowie/Qwen3-8B-GPTQ-Int8
5	Llama-3.1-8B-Inst.	ModelCloud/Meta-Llama-3.1-8B-Instruct-gptq-4bit
6	Ministral-3-Inst.	—
7	DeepSeek-R1-Distill	jakiAJK/DeepSeek-R1-Distill-Llama-8B-GPTQ-int4

E.4 GGUF repositories

Table 8 lists the GGUF repositories and filename conventions for each model. GGUF files follow one of two naming conventions depending on the repository provider: *dot convention* (Model.Q4_K_M.gguf) used by QuantFactory and mradermacher, or *dash convention* (Model-Q4_K_M.gguf) used by Qwen, bartowski, and most official releases.

Table 8: GGUF repositories and filename templates. Each repository provides quants Q8_0, Q6_K, Q5_K_M, Q4_K_M, Q3_K_M, and Q2_K unless otherwise noted.

#	Model	GGUF Repository	Filename Template
1	Qwen3-8B-Base	mradermacher/Qwen3-8B-Base-GGUF	Qwen3-8B-Base.{Q}.gguf
2	Llama-3.1-8B	QuantFactory/Meta-Llama-3.1-8B-GGUF	Meta-Llama-3.1-8B.{Q}.gguf
3	Ministral-3-Base	mradermacher/Ministral-3-8B-Base-2512-GGUF	Ministral-3-8B-Base-2512.{Q}.gguf
4	Qwen3-8B	Qwen/Qwen3-8B-GGUF	Qwen3-8B-{Q}.gguf
5	Llama-3.1-8B-Inst.	bartowski/Meta-Llama-3.1-8B-Instruct-GGUF	...-Instruct-{Q}.gguf
6	Ministral-3-Inst.	bartowski/mistralai_Ministral-3-8B-Instruct-2512-GGUF	...-2512-{Q}.gguf
7	DeepSeek-R1-Distill	bartowski/DeepSeek-R1-Distill-Llama-8B-GGUF	...-Llama-8B-{Q}.gguf

E.5 Backend coverage summary

Table 9 provides a per-model summary of quantization backend coverage across the combinations we evaluated.

Table 9: Quantization backend coverage per model. ✓ = included in our experiments; — = not evaluated in this study.

#	Model	BnB	GGUF	GPTQ
1	Qwen3-8B-Base	✓	✓	—
2	Llama-3.1-8B	✓	✓	✓
3	Ministral-3-8B-Base	✓	✓	—
4	Qwen3-8B	✓	✓	✓
5	Llama-3.1-8B-Instruct	✓	✓	✓
6	Ministral-3-8B-Instruct	✓	✓	—
7	DeepSeek-R1-Distill-Llama	✓	✓	✓
Total		7/7	7/7	4/7

Experiment scope. Each model is evaluated on the backend/bit-width combinations marked ✓ in Table 9: GGUF (6 bit-widths) and BitsAndBytes (3 configurations) on every model, plus the GPTQ checkpoint listed in Table 7 where available. The cells marked “—” are outside our experiment scope under the compute and time budget for this study.

F Quantization replication, feature-only scatter, and per-model tables

F.1 Replication on Ministral and DeepSeek

Figure 5 replicates the main quantization scatter (Fig. 2) on the two additional 8B families—Ministral-3-8B and DeepSeek-R1-Distill-Llama-8B—kept out of the main text for symmetry with the LoRA experiments (Sec. 5.1). The bound tracks $|\Delta\mathcal{R}|$ on these two families with patterns consistent with the Llama–Qwen main analysis, supporting the cross-family generality of the PRISM framework. Per-variant numerical decompositions for all four families are in Appendix F.3.

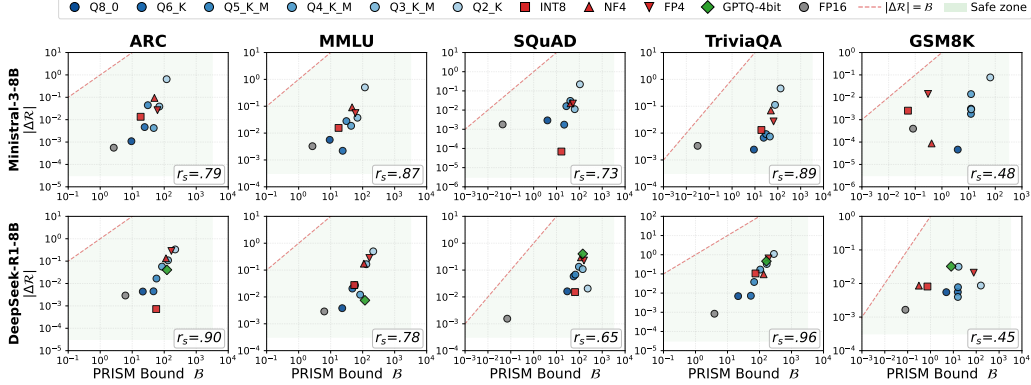


Figure 5: **PTQ replication on Ministral-3-8B and DeepSeek-R1-Distill-Llama-8B.** Counterpart of main-text Fig. 2 (Llama-3.1-8B and Qwen3-8B), with identical axes, PTQ family color coding, and benchmark set. Rows: Ministral-3-8B, DeepSeek-R1-Distill-Llama-8B. Columns: ARC, MMLU, SQuAD, TriviaQA, GSM8K. Per-subplot Spearman r_s is annotated in each panel.

F.2 Feature-only scatter

Figure 6 reports the feature-alignment-only replication of the main quantization result (Fig. 2), with the x-axis replaced by the head-free term $\delta = K_{\text{feat}} \sqrt{(\rho_T - \rho_P)^2 + 2\rho_T\rho_P(1 - \Omega)}$. The grid isolates the backbone contribution to the bound and is the source of the aggregate feature-only correlation $\bar{r}_s(\delta)$ cited in Sec. 5.2.

F.3 Per-model decomposition tables

We report the full geometric decomposition (Eq. 2) for each evaluated model, covering all quantization variants and benchmarks. Each table column lists the base RMS scale ρ_T , proxy RMS scale ρ_P , identity-alignment similarity Ω , feature alignment error δ , head discrepancy γ , full PRISM bound \mathcal{B} , and empirical cross-entropy gap $|\Delta\mathcal{R}|$. Per-dataset Spearman rank correlations $r_s(\delta, |\Delta\mathcal{R}|)$ appear in the left-hand column of each benchmark block.

The base-model tables cover the four 8B families: Llama-3.1-8B extended benchmarks in Table 11, Ministral-3-8B in Table 13, Qwen3-8B in Table 12 (also referenced in Sec. 5.3), and DeepSeek-R1-Distill-Llama-8B in Table 14. The instruction-tuned counterparts of Llama, Ministral, and Qwen are reported in Tables 15, 17, and 16 respectively, and reproduce the same patterns as their base counterparts. Across ARC/MMLU/SQuAD/TriviaQA the per-benchmark mean Spearman lies in $r_s \in [0.77, 0.89]$ (Table 10); GSM8K is the weakest benchmark across families ($r_s \approx 0.41$) because its long teacher-forced chain-of-thought answer spans dilute per-token loss, shrinking mean $|\Delta\mathcal{R}|$ to ≈ 0.019 —an order of magnitude below the other benchmarks (0.07–0.16). For Qwen3-8B-Instruct in particular the mean $|\Delta\mathcal{R}|$ on GSM8K is only 0.0033; at this scale, per-variant differences are dominated by measurement noise rather than the bound’s predictive signal.

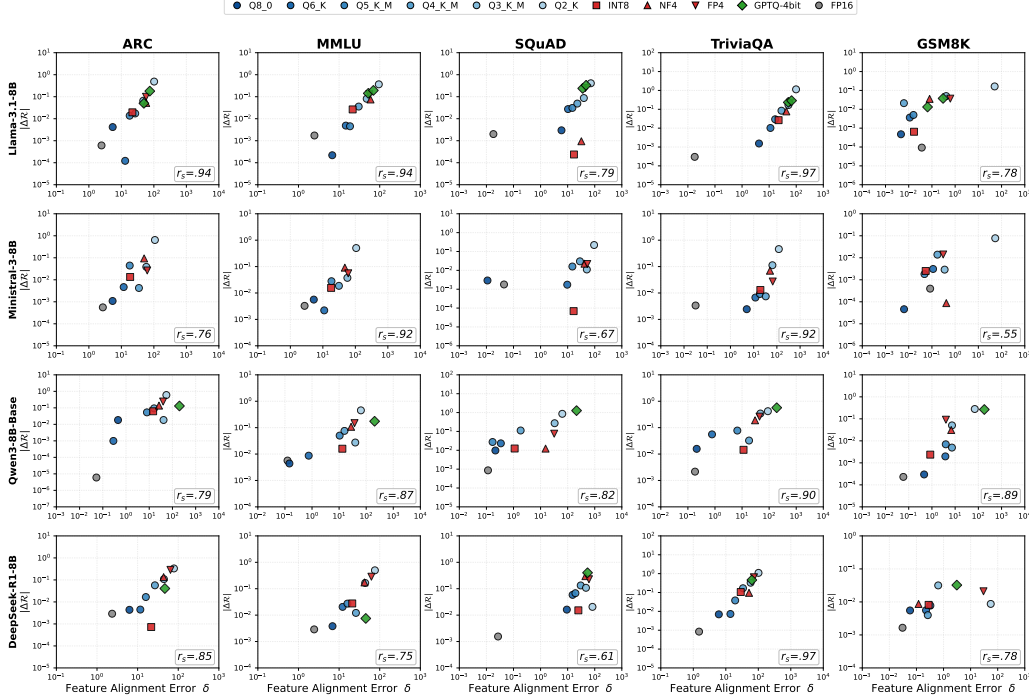


Figure 6: **Feature alignment error δ alone is already highly predictive of the risk gap.** Identical layout to Fig. 2 but with x-axis replaced by the feature-only term δ . Because most protocols retain the $1m_head$ in FP16, the head-discrepancy term γ is zero for GPTQ and BitsAndBytes and small for GGUF configurations that quantize output embeddings; δ therefore captures most of the predictive signal of Fig. 2, confirming that scale collapse $(\Delta\rho)^2$ and shape mismatch $(1 - \Omega)$ are the dominant degradation channels under PTQ (Sec. 4).

Table 11: Geometric decomposition for **Llama-3.1-8B** under identity alignment ($W=I$) on extended benchmarks (excl. MMLU). Each benchmark section reports Spearman’s $r_s(\mathcal{B}, |\Delta\mathcal{R}|)$ across all quantization variants. Shading: $\Omega < 0.80$ / $\Omega < 0.95$ on $(\Omega, \delta, \mathcal{B}, |\Delta\mathcal{R}|)$; $\gamma=0$ when the head is preserved ($H_T=H_P$).

Dataset	Family	Method	ρ_T	ρ_P	Ω	δ	γ	PRISM \mathcal{B}	$ \Delta\mathcal{R} $	
ARC ($r_s=0.94$)	-	FP16	137.58	137.63	0.9998	6.4005	0	6.4005	0.0006	
		GGUF	Q8_0	137.58	137.68	0.9992	14.1298	5.4302	19.5600	0.0042
			Q6_K	137.58	138.13	0.9955	34.2057	17.0429	51.2485	0.0001
			Q5_K_M	137.58	138.57	0.9915	47.1100	17.1085	64.2184	0.0137
			Q4_K_M	137.58	137.71	0.9812	69.7158	17.0069	86.7227	0.0173
			Q3_K_M	137.58	138.68	0.9420	123.0240	17.0915	140.1155	0.0654
			Q2_K	137.58	144.67	0.7408	266.1578	17.9731	284.1309	0.4877
		BnB	INT8	137.58	137.99	0.9874	57.1279	0	57.1279	0.0195
			NF4	137.58	142.78	0.9155	151.2430	0	151.2430	0.0523
			FP4	137.58	135.87	0.9117	150.2742	0	150.2742	0.0992
	GPTQ	GPTQ-4bit	137.58	138.70	0.9363	128.9004	0	128.9004	0.0501	
TriviaQA ($r_s=0.97$)	-	FP16	140.93	140.91	1.0000	0.0467	0	0.0467	0.0003	
		GGUF	Q8_0	140.93	140.89	0.9996	11.0367	5.5270	16.5638	0.0015
			Q6_K	140.93	141.11	0.9969	29.2155	17.2531	46.4686	0.0102
			Q5_K_M	140.93	141.18	0.9930	43.5453	17.2612	60.8066	0.0296
			Q4_K_M	140.93	141.14	0.9795	74.5725	17.2633	91.8357	0.0842
			Q3_K_M	140.93	141.39	0.9330	135.0997	17.3007	152.4004	0.1675
			Q2_K	140.93	142.25	0.7574	257.7881	17.4123	275.2004	1.1405
		BnB	INT8	140.93	141.07	0.9875	58.3674	0	58.3674	0.0266
			NF4	140.93	142.03	0.9533	113.0393	0	113.0393	0.0773

continued on next page

(continued from previous page)

Dataset	Family	Method	ρ_T	ρ_P	Ω	δ	γ	PRISM \mathcal{B}	$ \Delta\mathcal{R} $
	GPTQ	FP4	140.93	142.54	0.9124	155.0800	0	155.0800	0.2248
		GPTQ-4bit	140.93	141.30	0.9347	133.2628	0	133.2628	0.2326
SQuAD ($r_s=0.81$)	GGUF	FP16	138.24	138.22	1.0000	0.0473	0	0.0474	0.0020
		Q8_0	138.24	138.17	0.9991	15.4689	5.3498	20.8187	0.0030
		Q6_K	138.24	138.21	0.9972	26.9698	16.8428	43.8126	0.0274
		Q5_K_M	138.24	138.17	0.9941	39.1050	16.8350	55.9400	0.0310
		Q4_K_M	138.24	138.17	0.9865	59.4253	16.8380	76.2632	0.0488
		Q3_K_M	138.24	138.24	0.9589	103.5452	16.8464	120.3916	0.0870
	BnB	Q2_K	138.24	138.53	0.8655	187.6258	16.8715	204.4973	0.4090
		INT8	138.24	138.14	0.9924	44.6233	0	44.6233	0.0002
		NF4	138.24	138.33	0.9731	83.7629	0	83.7629	0.0009
		FP4	138.24	139.19	0.9466	118.5596	0	118.5596	0.2508
GPTQ	GPTQ-4bit	138.24	138.33	0.9663	93.8623	0	93.8623	0.2382	
GSM8K ($r_s=0.51$)	GGUF	FP16	134.24	134.28	1.0000	0.0956	0	0.0956	0.0001
		Q8_0	134.24	134.24	1.0000	0.0121	5.3871	5.3992	0.0005
		Q6_K	134.24	134.23	1.0000	0.0291	16.9360	16.9652	0.0036
		Q5_K_M	134.24	134.26	1.0000	0.0418	16.9378	16.9797	0.0050
		Q4_K_M	134.24	134.24	1.0000	0.0162	16.9326	16.9488	0.0211
		Q3_K_M	134.24	134.65	1.0000	1.0723	16.9967	18.0690	0.0502
	BnB	Q2_K	134.24	134.51	0.9298	131.5907	16.9517	148.5423	0.1630
		INT8	134.24	134.22	1.0000	0.0441	0	0.0441	0.0006
		NF4	134.24	134.32	1.0000	0.2076	0	0.2076	0.0356
		FP4	134.24	134.86	1.0000	1.6168	0	1.6168	0.0367
GPTQ	GPTQ-4bit	134.24	134.18	1.0000	0.1695	0	0.1695	0.0132	

Table 12: Geometric decomposition for **Qwen3-8B-Base** under identity alignment ($W=I$) on all benchmarks. Each benchmark section reports Spearman’s $r_s(\mathcal{B}, |\Delta\mathcal{R}|)$ across all quantization variants. Shading: $\Omega < 0.80$ / $\Omega < 0.95$ on $(\Omega, \delta, \mathcal{B}, |\Delta\mathcal{R}|)$; $\gamma=0$ when the head is preserved ($H_T=H_P$).

Dataset	Family	Method	ρ_T	ρ_P	Ω	δ	γ	PRISM \mathcal{B}	$ \Delta\mathcal{R} $
MMLU ($r_s=0.84$)	GGUF	FP16	332.87	333.00	1.0000	0.4310	0	0.4310	0.0057
		Q8_0	332.87	332.73	1.0000	0.5059	26.8061	27.3120	0.0044
		Q6_K	332.87	332.12	1.0000	2.6076	85.0765	87.6841	0.0087
		Q5_K_M	332.87	332.02	0.9995	36.2699	85.0170	121.2869	0.0500
		Q4_K_M	332.87	333.30	0.9989	54.6755	85.3799	140.0554	0.0754
		Q3_K_M	332.87	324.42	0.9931	136.6995	82.9287	219.6281	0.0274
	BnB	Q2_K	332.87	336.88	0.9819	220.4909	86.2315	306.7224	0.4521
		INT8	332.87	332.24	0.9992	45.5886	0	45.5886	0.0159
		NF4	332.87	329.71	0.9966	95.6438	0	95.6438	0.1076
FP4	332.87	332.87	0.9938	128.4300	0	128.4300	0.1483		
ARC ($r_s=0.65$)	GGUF	FP16	332.71	332.77	1.0000	0.1830	0	0.1831	0.0000
		Q8_0	332.71	332.26	1.0000	1.5660	26.7533	28.3194	0.0183
		Q6_K	332.71	332.43	1.0000	0.9876	85.0956	86.0832	0.0010
		Q5_K_M	332.71	333.21	0.9997	27.5096	85.2474	112.7570	0.0533
		Q4_K_M	332.71	333.72	0.9988	56.0316	85.3776	141.4092	0.0932
		Q3_K_M	332.71	319.87	0.9927	143.1645	81.5376	224.7021	0.0184
	BnB	Q2_K	332.71	338.59	0.9869	189.1571	86.5945	275.7516	0.5978
		INT8	332.71	329.14	0.9991	50.9372	0	50.9372	0.0620
		NF4	332.71	328.25	0.9969	91.0051	0	91.0051	0.1367
FP4	332.71	333.50	0.9929	137.3760	0	137.3760	0.2419		
TriviaQA ($r_s=0.94$)	GGUF	FP16	241.01	240.83	1.0000	0.6337	0	0.6338	0.0022
		Q8_0	241.01	241.22	1.0000	0.7309	18.9698	19.7007	0.0158
		Q6_K	241.01	241.79	1.0000	2.6885	60.1070	62.7955	0.0556

continued on next page

(continued from previous page)

Dataset	Family	Method	ρ_T	ρ_P	Ω	δ	γ	PRISM \mathcal{B}	$ \Delta\mathcal{R} $	
	BnB	Q5_K_M	241.01	239.98	0.9996	23.1271	59.5715	82.6986	0.0776	
		Q4_K_M	241.01	241.74	0.9972	62.6955	60.0594	122.7549	0.0325	
		Q3_K_M	241.01	235.11	0.9804	164.3962	58.0817	222.4779	0.3429	
		Q2_K	241.01	253.07	0.9351	310.5940	63.4073	374.0012	0.4199	
		INT8	241.01	239.25	0.9989	39.2009	0	39.2009	0.0145	
		NF4	241.01	241.11	0.9921	104.6219	0	104.6219	0.1900	
		FP4	241.01	241.03	0.9832	152.7570	0	152.7570	0.2615	
SQuAD ($r_s=0.95$)	-	FP16	298.04	297.92	1.0000	0.3954	0	0.3954	0.0009	
		GGUF	Q8_0	298.04	298.25	1.0000	0.7419	23.9590	24.7008	0.0098
		Q6_K	298.04	298.38	1.0000	1.1798	75.7671	76.9469	0.0234	
		Q5_K_M	298.04	297.87	1.0000	0.5839	75.6329	76.2168	0.0275	
	BnB	Q4_K_M	298.04	299.88	1.0000	6.3512	76.1849	82.5360	0.1121	
		Q3_K_M	298.04	297.59	0.9938	114.2894	75.4513	189.7407	0.2722	
		Q2_K	298.04	307.56	0.9786	219.0695	78.2900	297.3595	0.8582	
		INT8	298.04	296.94	1.0000	3.8134	0	3.8134	0.0124	
		NF4	298.04	292.80	0.9988	52.9278	0	52.9278	0.0123	
		FP4	298.04	304.82	0.9947	110.2163	0	110.2163	0.0758	
GSM8K ($r_s=0.68$)	-	FP16	267.17	267.23	1.0000	0.2028	0	0.2028	0.0002	
		GGUF	Q8_0	267.17	266.71	1.0000	1.5944	21.6634	23.2578	0.0003
		Q6_K	267.17	270.95	1.0000	13.0938	69.4224	82.5161	0.0020	
		Q5_K_M	267.17	271.11	1.0000	13.6428	69.4669	83.1096	0.0070	
	BnB	Q4_K_M	267.17	274.46	1.0000	25.2256	70.3239	95.5495	0.0049	
		Q3_K_M	267.17	274.49	1.0000	25.3174	70.2868	95.6042	0.0504	
		Q2_K	267.17	313.41	0.9835	242.2547	80.5797	322.8344	0.2799	
		INT8	267.17	268.01	1.0000	2.9317	0	2.9317	0.0024	
		NF4	267.17	273.95	1.0000	23.4507	0	23.4507	0.0309	
		FP4	267.17	271.17	1.0000	13.8517	0	13.8517	0.0915	

Table 13: Geometric decomposition for **Ministral-3-8B-Base** under identity alignment ($W=I$) on all benchmarks. Each benchmark section reports Spearman’s $r_s(\mathcal{B}, |\Delta\mathcal{R}|)$ across all quantization variants. Shading: $\Omega < 0.80$ / $\Omega < 0.95$ on $(\Omega, \delta, \mathcal{B}, |\Delta\mathcal{R}|)$; $\gamma = 0$ when the head is preserved ($H_T = H_P$).

Dataset	Family	Method	ρ_T	ρ_P	Ω	δ	γ	PRISM \mathcal{B}	$ \Delta\mathcal{R} $	
MMLU ($r_s=0.87$)	-	FP16	191.06	191.04	0.9999	2.6982	0	2.6983	0.0033	
		GGUF	Q8_0	191.06	191.04	0.9996	5.1801	4.1685	9.3485	0.0056
		Q6_K	191.06	191.13	0.9983	10.8538	12.9094	23.7632	0.0022	
		Q5_K_M	191.06	191.55	0.9954	18.1440	12.9197	31.0637	0.0280	
	BnB	Q4_K_M	191.06	191.12	0.9867	30.7499	12.8820	43.6318	0.0187	
		Q3_K_M	191.06	190.43	0.9555	56.0293	12.8388	68.8680	0.0374	
		Q2_K	191.06	193.99	0.8483	104.4697	13.0266	117.4963	0.5035	
		INT8	191.06	191.21	0.9956	17.6961	0	17.6961	0.0156	
		NF4	191.06	190.92	0.9691	46.7819	0	46.7819	0.0910	
		FP4	191.06	191.57	0.9503	59.3922	0	59.3922	0.0558	
ARC ($r_s=0.79$)	-	FP16	191.14	191.11	0.9999	2.6480	0	2.6480	0.0006	
		GGUF	Q8_0	191.14	191.06	0.9996	5.2859	4.1436	9.4295	0.0011
		Q6_K	191.14	191.08	0.9981	11.6035	12.8801	24.4836	0.0047	
		Q5_K_M	191.14	191.55	0.9955	17.7885	12.9031	30.6917	0.0443	
	BnB	Q4_K_M	191.14	190.56	0.9835	34.1959	12.8217	47.0176	0.0042	
		Q3_K_M	191.14	189.89	0.9529	57.5874	12.7906	70.3780	0.0387	
		Q2_K	191.14	194.14	0.8439	106.0342	12.9650	118.9992	0.6424	
		INT8	191.14	191.46	0.9953	18.3240	0	18.3240	0.0135	
		NF4	191.14	190.54	0.9655	49.4023	0	49.4023	0.0936	
FP4	191.14	191.92	0.9468	61.5350	0	61.5350	0.0265			

continued on next page

(continued from previous page)

Dataset	Family	Method	ρ_T	ρ_P	Ω	δ	γ	PRISM \mathcal{B}	$ \Delta\mathcal{R} $	
TriviaQA ($r_s=0.89$)	-	FP16	194.05	194.02	1.0000	0.0310	0	0.0311	0.0034	
		GGUF	Q8_0	194.05	194.07	0.9997	4.9601	4.0564	9.0165	0.0024
			Q6_K	194.05	194.09	0.9981	11.7063	12.4435	24.1498	0.0067
			Q5_K_M	194.05	194.13	0.9954	18.3912	12.4407	30.8319	0.0092
			Q4_K_M	194.05	194.23	0.9854	32.6582	12.4456	45.1038	0.0075
	Q3_K_M		194.05	193.98	0.9452	63.2523	12.4345	75.6868	0.1125	
	BnB	Q2_K	194.05	195.16	0.8057	119.4909	12.5116	132.0025	0.4595	
		INT8	194.05	194.15	0.9950	19.1477	0	19.1477	0.0130	
		NF4	194.05	194.10	0.9661	49.7942	0	49.7942	0.0697	
		FP4	194.05	194.43	0.9417	65.3043	0	65.3043	0.0272	
SQuAD ($r_s=0.73$)		-	FP16	186.67	186.62	1.0000	0.0440	0	0.0440	0.0018
GGUF	Q8_0		186.67	186.68	1.0000	0.0108	3.9943	4.0050	0.0029	
	Q6_K		186.67	186.66	0.9987	9.5143	12.1987	21.7130	0.0017	
	Q5_K_M		186.67	186.60	0.9968	14.7202	12.1942	26.9145	0.0160	
	Q4_K_M		186.67	186.82	0.9885	27.9430	12.1948	40.1377	0.0302	
	Q3_K_M		186.67	186.89	0.9626	50.2928	12.2120	62.5048	0.0111	
BnB	Q2_K		186.67	188.53	0.8724	93.3676	12.2665	105.6341	0.2206	
	INT8		186.67	186.71	0.9960	16.3442	0	16.3442	0.0001	
	NF4		186.67	186.50	0.9748	41.2389	0	41.2389	0.0226	
	FP4		186.67	187.23	0.9598	52.2330	0	52.2330	0.0219	
	GSM8K ($r_s=0.48$)	-	FP16	179.04	179.13	1.0000	0.0826	0	0.0826	0.0004
GGUF	Q8_0		179.04	179.05	1.0000	0.0062	3.9076	3.9138	0.0000	
	Q6_K		179.04	178.93	1.0000	0.1107	12.1709	12.2816	0.0031	
	Q5_K_M		179.04	179.00	1.0000	0.0470	12.1743	12.2213	0.0018	
	Q4_K_M		179.04	179.22	1.0000	0.1696	12.1799	12.3495	0.0139	
	Q3_K_M		179.04	179.40	1.0000	0.3472	12.1980	12.5452	0.0029	
BnB	Q2_K		179.04	181.13	0.9561	52.5668	12.2589	64.8258	0.0772	
	INT8		179.04	179.10	1.0000	0.0531	0	0.0531	0.0025	
	NF4		179.04	178.63	1.0000	0.4096	0	0.4096	0.0001	
	FP4		179.04	179.35	1.0000	0.3011	0	0.3011	0.0141	

Table 14: Geometric decomposition for **DeepSeek-R1-Distill-Llama-8B** under identity alignment ($W=I$) on all benchmarks. Each benchmark section reports Spearman’s $r_s(\mathcal{B}, |\Delta\mathcal{R}|)$ across all quantization variants. Shading: $\Omega < 0.80$ / $\Omega < 0.95$ on $(\Omega, \delta, \mathcal{B}, |\Delta\mathcal{R}|)$; $\gamma = 0$ when the head is preserved ($H_T = H_P$).

Dataset	Family	Method	ρ_T	ρ_P	Ω	δ	γ	PRISM \mathcal{B}	$ \Delta\mathcal{R} $	
MMLU ($r_s=0.78$)	-	FP16	130.42	130.30	0.9998	6.3231	0	6.3231	0.0029	
		GGUF	Q8_0	130.42	130.04	0.9986	17.8882	5.1177	23.0059	0.0038
			Q6_K	130.42	130.50	0.9956	31.7135	16.0293	47.7428	0.0205
			Q5_K_M	130.42	130.31	0.9925	41.6249	16.0159	57.6408	0.0273
			Q4_K_M	130.42	130.73	0.9802	67.4996	16.0775	83.5772	0.0121
	Q3_K_M		130.42	133.80	0.9452	113.9650	16.4417	130.4067	0.1651	
	BnB	Q2_K	130.42	134.51	0.8355	197.7487	16.4049	214.1535	0.4977	
		INT8	130.42	131.30	0.9871	54.7277	0	54.7277	0.0277	
		NF4	130.42	133.20	0.9490	109.6652	0	109.6652	0.1732	
		FP4	130.42	135.19	0.8903	162.1313	0	162.1313	0.2850	
GPTQ		GPTQ-4bit	130.42	132.77	0.9407	117.9387	0	117.9387	0.0075	
ARC ($r_s=0.90$)	-	FP16	129.06	129.02	0.9998	6.1255	0	6.1255	0.0029	
		GGUF	Q8_0	129.06	128.80	0.9988	16.3476	5.0448	21.3925	0.0044
			Q6_K	129.06	129.14	0.9959	30.2995	15.8091	46.1087	0.0045
			Q5_K_M	129.06	128.92	0.9924	41.4248	15.7913	57.2161	0.0167
			Q4_K_M	129.06	130.23	0.9789	69.2502	15.9862	85.2364	0.0569
			Q3_K_M	129.06	133.12	0.9431	115.3662	16.3273	131.6935	0.1086

continued on next page

(continued from previous page)

Dataset	Family	Method	ρ_T	ρ_P	Ω	δ	γ	PRISM \mathcal{B}	$ \Delta\mathcal{R} $	
	BnB	Q2_K	129.06	134.02	0.8228	203.9118	16.3259	220.2377	0.3327	
		INT8	129.06	129.36	0.9861	56.0644	0	56.0644	0.0007	
		NF4	129.06	132.28	0.9445	113.4221	0	113.4221	0.1337	
		FP4	129.06	135.34	0.8825	167.3408	0	167.3408	0.2866	
	GPTQ	GPTQ-4bit	129.06	132.05	0.9360	121.6208	0	121.6208	0.0407	
TriviaQA ($r_s=0.96$)	–	FP16	143.70	143.66	0.9999	3.9059	0	3.9060	0.0008	
		GGUF	Q8_0	143.70	143.69	0.9991	15.8440	5.6723	21.5163	0.0069
		Q6_K	143.70	143.67	0.9953	36.0293	17.5786	53.6079	0.0073	
		Q5_K_M	143.70	143.78	0.9909	50.4752	17.5929	68.0682	0.0379	
		Q4_K_M	143.70	143.71	0.9724	87.8327	17.5827	105.4155	0.1682	
		Q3_K_M	143.70	144.10	0.9186	150.9221	17.6260	168.5481	0.3294	
		Q2_K	143.70	144.13	0.7515	263.7237	17.6317	281.3554	1.0967	
	BnB	INT8	143.70	143.85	0.9799	74.9114	0	74.9114	0.1057	
		NF4	143.70	143.85	0.9351	134.6541	0	134.6541	0.0959	
		FP4	143.70	144.30	0.8696	191.1589	0	191.1589	0.6411	
	GPTQ	GPTQ-4bit	143.70	144.14	0.9032	164.5533	0	164.5533	0.4587	
	SQuAD ($r_s=0.65$)	–	FP16	133.98	133.95	1.0000	0.0699	0	0.0699	0.0015
			GGUF	Q8_0	133.98	133.97	0.9976	24.2320	5.2141	29.4460
Q6_K			133.98	133.75	0.9935	39.5629	16.4516	56.0145	0.0584	
Q5_K_M			133.98	133.78	0.9896	50.1989	16.4562	66.6551	0.0677	
Q4_K_M			133.98	133.72	0.9743	78.8687	16.4442	95.3129	0.1332	
Q3_K_M			133.98	134.76	0.9376	123.3841	16.5499	139.9340	0.1084	
Q2_K			133.98	135.89	0.8134	214.2984	16.6592	230.9575	0.0205	
BnB		INT8	133.98	134.24	0.9829	64.5345	0	64.5345	0.0152	
		NF4	133.98	134.33	0.9430	117.6838	0	117.6838	0.2994	
		FP4	133.98	135.37	0.8972	158.7895	0	158.7895	0.2282	
GPTQ		GPTQ-4bit	133.98	137.60	0.9206	140.9024	0	140.9024	0.4021	
GSM8K ($r_s=0.45$)		–	FP16	120.55	120.52	1.0000	0.0796	0	0.0797	0.0017
			GGUF	Q8_0	120.55	120.49	1.0000	0.1506	4.7556	4.9062
	Q6_K		120.55	120.32	1.0000	0.5861	15.0761	15.6622	0.0056	
	Q5_K_M		120.55	120.22	1.0000	0.8500	15.0619	15.9119	0.0077	
	Q4_K_M		120.55	120.29	1.0000	0.6819	15.0733	15.7552	0.0040	
	Q3_K_M		120.55	121.18	1.0000	1.6511	15.2217	16.8727	0.0316	
	Q2_K		120.55	122.39	0.8963	143.8615	15.3978	159.2594	0.0087	
	BnB	INT8	120.55	120.83	1.0000	0.7327	0	0.7327	0.0081	
		NF4	120.55	120.67	1.0000	0.3110	0	0.3110	0.0086	
		FP4	120.55	122.26	0.9697	77.7554	0	77.7554	0.0210	
	GPTQ	GPTQ-4bit	120.55	123.64	1.0000	8.0360	0	8.0360	0.0323	

Table 15: Geometric decomposition for **Llama-3.1-8B-Instruct** under identity alignment ($W=I$) on all benchmarks. Each benchmark section reports Spearman’s $r_s(\mathcal{B}, |\Delta\mathcal{R}|)$ across all quantization variants. Shading: $\Omega < 0.80$ / $\Omega < 0.95$ on $(\Omega, \delta, \mathcal{B}, |\Delta\mathcal{R}|)$; $\gamma = 0$ when the head is preserved ($H_T = H_P$).

Dataset	Family	Method	ρ_T	ρ_P	Ω	δ	γ	PRISM \mathcal{B}	$ \Delta\mathcal{R} $	
MMLU ($r_s=0.71$)	–	FP16	144.62	144.62	0.9997	9.0568	0	9.0568	0.0006	
		GGUF	Q8_0	144.62	144.53	0.9954	35.9084	5.6784	41.5868	0.0225
		Q6_K	144.62	144.62	0.9923	46.6172	17.6498	64.2670	0.0147	
		Q5_K_M	144.62	144.62	0.9851	65.0189	17.6591	82.6780	0.0134	
		Q4_K_M	144.62	143.11	0.9401	129.5315	17.3881	146.9196	0.1047	
	Q3_K_M	144.62	141.90	0.8548	200.8720	17.2517	218.1237	0.0306		
	Q2_K	144.62	144.24	0.7331	274.3785	17.6133	291.9918	0.6372		
	BnB	INT8	144.62	144.44	0.9771	80.4019	0	80.4019	0.0423	
		NF4	144.62	145.41	0.9155	155.0510	0	155.0510	0.1038	
FP4		144.62	144.77	0.8618	197.7782	0	197.7782	0.0551		

continued on next page

(continued from previous page)

Dataset	Family	Method	ρ_T	ρ_P	Ω	δ	γ	PRISM \mathcal{B}	$ \Delta\mathcal{R} $
	GPTQ	GPTQ-4bit	144.62	143.76	0.8708	190.6339	0	190.6339	0.0867
ARC ($r_s=0.53$)	–	FP16	145.60	145.61	0.9995	12.3411	0	12.3411	0.0001
	GGUF	Q8_0	145.60	145.61	0.9970	29.1756	5.7418	34.9174	0.0107
		Q6_K	145.60	145.68	0.9934	43.4717	17.8881	61.3598	0.0144
		Q5_K_M	145.60	145.69	0.9879	58.8497	17.9008	76.7505	0.0141
		Q4_K_M	145.60	145.17	0.9592	108.0466	17.7797	125.8263	0.0028
		Q3_K_M	145.60	143.71	0.8828	182.1911	17.6230	199.8141	0.0103
	BnB	Q2_K	145.60	145.45	0.7456	269.9120	17.7991	287.7111	0.4741
		INT8	145.60	145.49	0.9795	76.5661	0	76.5661	0.0199
		NF4	145.60	146.24	0.9204	151.4443	0	151.4443	0.0432
		FP4	145.60	146.18	0.8657	196.6353	0	196.6353	0.0798
GPTQ	GPTQ-4bit	145.60	145.43	0.8796	185.6726	0	185.6726	0.0119	
TriviaQA ($r_s=0.97$)	–	FP16	143.91	143.91	1.0000	0.0037	0	0.0037	0.0010
	GGUF	Q8_0	143.91	143.95	0.9994	12.6885	5.6520	18.3405	0.0021
		Q6_K	143.91	144.01	0.9969	29.6264	17.4955	47.1219	0.0210
		Q5_K_M	143.91	143.91	0.9926	45.5890	17.4801	63.0692	0.0654
		Q4_K_M	143.91	144.00	0.9781	78.3518	17.4988	95.8505	0.0653
		Q3_K_M	143.91	144.32	0.9288	141.4285	17.5455	158.9739	0.3116
	BnB	Q2_K	143.91	145.04	0.7730	253.1214	17.6629	270.7843	1.0636
		INT8	143.91	144.33	0.9843	66.4209	0	66.4209	0.0496
		NF4	143.91	144.84	0.9450	124.5222	0	124.5222	0.1588
		FP4	143.91	144.93	0.9044	164.2065	0	164.2065	0.3070
GPTQ	GPTQ-4bit	143.91	144.13	0.9331	136.9950	0	136.9950	0.1271	
SQuAD ($r_s=0.90$)	–	FP16	138.74	138.71	1.0000	0.0693	0	0.0693	0.0002
	GGUF	Q8_0	138.74	138.76	0.9991	15.0126	5.3489	20.3615	0.0031
		Q6_K	138.74	138.79	0.9976	24.8796	16.7791	41.6587	0.0171
		Q5_K_M	138.74	138.77	0.9953	34.8378	16.7760	51.6138	0.0095
		Q4_K_M	138.74	138.89	0.9873	57.5090	16.7938	74.3028	0.0198
		Q3_K_M	138.74	138.92	0.9672	92.4334	16.7992	109.2326	0.0664
	BnB	Q2_K	138.74	138.30	0.8992	161.7335	16.7209	178.4544	0.3098
		INT8	138.74	138.72	0.9921	45.2550	0	45.2550	0.0130
		NF4	138.74	138.83	0.9693	89.3699	0	89.3699	0.0479
		FP4	138.74	139.36	0.9459	118.9474	0	118.9474	0.1904
GPTQ	GPTQ-4bit	138.74	138.89	0.9665	93.3836	0	93.3836	0.0678	
GSM8K ($r_s=0.45$)	–	FP16	134.52	134.54	1.0000	0.0545	0	0.0546	0.0004
	GGUF	Q8_0	134.52	134.54	1.0000	0.0633	5.3512	5.4146	0.0007
		Q6_K	134.52	134.48	1.0000	0.0905	16.7892	16.8796	0.0019
		Q5_K_M	134.52	134.56	1.0000	0.0993	16.7999	16.8992	0.0087
		Q4_K_M	134.52	134.22	1.0000	0.7816	16.7575	17.5391	0.0028
		Q3_K_M	134.52	134.67	1.0000	0.3912	16.8052	17.1965	0.0215
	BnB	Q2_K	134.52	133.96	0.9129	145.7227	16.7320	162.4548	0.1025
		INT8	134.52	134.54	1.0000	0.0608	0	0.0608	0.0046
		NF4	134.52	134.43	1.0000	0.2252	0	0.2252	0.0274
		FP4	134.52	134.92	0.9815	67.4488	0	67.4488	0.0217
GPTQ	GPTQ-4bit	134.52	134.95	1.0000	1.1173	0	1.1173	0.0302	

Table 16: Geometric decomposition for **Qwen3-8B-Instruct** under identity alignment ($W=I$) on all benchmarks. Each benchmark section reports Spearman’s $r_s(\mathcal{B}, |\Delta\mathcal{R}|)$ across all quantization variants. Shading: $\Omega < 0.80$ / $\Omega < 0.95$ on ($\Omega, \delta, \mathcal{B}, |\Delta\mathcal{R}|$); $\gamma=0$ when the head is preserved ($H_T=H_P$).

Dataset	Family	Method	ρ_T	ρ_P	Ω	δ	γ	PRISM \mathcal{B}	$ \Delta\mathcal{R} $
MMLU ($r_s=0.68$)	–	FP16	159.12	159.07	1.0000	0.1622	0	0.1622	0.0045
	GGUF	Q8_0	159.12	159.35	0.9997	12.2662	12.0379	24.3041	0.0013

continued on next page

(continued from previous page)

Dataset	Family	Method	ρ_T	ρ_P	Ω	δ	γ	PRISM \mathcal{B}	$ \Delta\mathcal{R} $	
	BnB	Q6_K	159.12	160.10	0.9979	35.6754	38.8644	74.5398	0.0219	
		Q5_K_M	159.12	159.94	0.9952	53.1786	38.8830	92.0616	0.0075	
		Q4_K_M	159.12	157.23	0.9888	80.8392	38.2293	119.0684	0.0812	
		INT8	159.12	161.47	0.9927	66.6772	0	66.6772	0.0537	
		NF4	159.12	161.29	0.9773	116.5416	0	116.5416	0.0214	
		FP4	159.12	161.12	0.9465	178.7626	0	178.7626	0.0455	
		GPTQ	GPTQ-8bit	159.12	158.63	0.9998	12.1107	0	12.1107	0.0027
ARC ($r_s=0.75$)	-	FP16	165.05	164.96	1.0000	0.3011	0	0.3012	0.0025	
		GGUF	Q8_0	165.05	165.00	0.9998	10.1008	12.5005	22.6013	0.0052
	BnB	Q6_K	165.05	165.43	0.9984	32.1931	40.2195	72.4126	0.0299	
		Q5_K_M	165.05	165.57	0.9962	48.9740	40.3151	89.2891	0.0046	
		Q4_K_M	165.05	163.96	0.9904	77.9990	39.8298	117.8288	0.0994	
		INT8	165.05	167.48	0.9934	65.7006	0	65.7006	0.0290	
		NF4	165.05	165.71	0.9776	119.2793	0	119.2793	0.0251	
		FP4	165.05	166.88	0.9531	173.4289	0	173.4289	0.1047	
	GPTQ	GPTQ-8bit	165.05	164.39	0.9998	10.4952	0	10.4952	0.0000	
	TriviaQA ($r_s=0.53$)	-	FP16	151.01	150.98	1.0000	0.0731	0	0.0731	0.0102
GGUF			Q8_0	151.01	151.12	0.9999	8.1868	11.0425	19.2294	0.0260
BnB		Q6_K	151.01	150.65	0.9975	36.1861	34.9084	71.0945	0.0351	
		Q5_K_M	151.01	151.41	0.9935	58.8856	35.0701	93.9557	0.0280	
		Q4_K_M	151.01	149.70	0.9820	97.4466	34.7298	132.1764	0.0152	
		INT8	151.01	151.53	0.9907	70.5433	0	70.5433	0.2055	
		NF4	151.01	153.15	0.9571	152.1411	0	152.1411	0.5815	
		FP4	151.01	151.49	0.9338	187.6604	0	187.6604	0.4596	
GPTQ	GPTQ-8bit	151.01	150.97	0.9999	8.1793	0	8.1793	0.0421		
SQuAD ($r_s=0.85$)	-	FP16	150.60	150.48	1.0000	0.4282	0	0.4282	0.0109	
		GGUF	Q8_0	150.60	150.60	1.0000	0.0234	11.1297	11.1531	0.0041
		Q6_K	150.60	149.92	0.9989	24.2100	35.2401	59.4501	0.0122	
		Q5_K_M	150.60	151.20	0.9954	49.3042	35.5707	84.8748	0.1442	
	BnB	Q4_K_M	150.60	150.24	0.9875	81.0862	35.3024	116.3885	0.1393	
		INT8	150.60	150.93	0.9928	61.7027	0	61.7027	0.0660	
		NF4	150.60	155.57	0.9656	137.9971	0	137.9971	0.2196	
		FP4	150.60	154.65	0.9500	165.0564	0	165.0564	0.1680	
GPTQ	GPTQ-8bit	150.60	150.59	1.0000	0.0350	0	0.0350	0.0143		
GSM8K ($r_s = -0.57$)	-	FP16	131.00	130.96	1.0000	0.1222	0	0.1223	0.0043	
		GGUF	Q8_0	131.00	131.00	1.0000	0.0088	10.0309	10.0397	0.0063
		Q6_K	131.00	130.47	1.0000	1.8182	31.9756	33.7938	0.0001	
		Q5_K_M	131.00	131.35	1.0000	1.2038	32.2172	33.4210	0.0043	
		Q4_K_M	131.00	128.35	1.0000	9.0309	31.5401	40.5710	0.0001	
	BnB	INT8	131.00	131.35	1.0000	1.2053	0	1.2053	0.0008	
		NF4	131.00	132.32	1.0000	4.5062	0	4.5062	0.0119	
		FP4	131.00	138.99	1.0000	27.2384	0	27.2384	0.0006	
GPTQ	GPTQ-8bit	131.00	130.86	1.0000	0.4622	0	0.4622	0.0017		

Table 17: Geometric decomposition for **Ministral-3-8B-Instruct** under identity alignment ($W=I$) on all benchmarks. Each benchmark section reports Spearman’s $r_s(\mathcal{B}, |\Delta\mathcal{R}|)$ across all quantization variants. Shading: $\Omega < 0.80$ / $\Omega < 0.95$ on $(\Omega, \delta, \mathcal{B}, |\Delta\mathcal{R}|)$; $\gamma = 0$ when the head is preserved ($H_T = H_P$).

Dataset	Family	Method	ρ_T	ρ_P	Ω	δ	γ	PRISM \mathcal{B}	$ \Delta\mathcal{R} $	
MMLU ($r_s=0.76$)	-	FP16	189.50	189.50	0.9999	2.1498	0	2.1498	0.0000	
		GGUF	Q8_0	189.50	189.43	0.9968	13.9973	3.9804	17.9777	0.0037
		Q6_K	189.50	189.44	0.9959	15.9304	12.3332	28.2635	0.0170	
		Q5_K_M	189.50	189.78	0.9936	19.9564	12.3393	32.2957	0.0267	

continued on next page

(continued from previous page)

Dataset	Family	Method	ρ_T	ρ_P	Ω	δ	γ	PRISM β	$ \Delta\mathcal{R} $	
	BnB	Q4_K_M	189.50	189.47	0.9835	31.9547	12.3388	44.2935	0.0119	
		Q3_K_M	189.50	187.06	0.9625	47.9109	12.2310	60.1419	0.0236	
		Q2_K	189.50	187.52	0.8842	84.2055	12.2532	96.4587	0.1117	
		INT8	189.50	189.33	0.9952	17.1379	0	17.1379	0.0101	
		NF4	189.50	189.63	0.9625	48.1985	0	48.1985	0.0066	
		FP4	189.50	189.18	0.9441	58.7507	0	58.7507	0.0564	
ARC ($r_s=0.81$)	-	FP16	189.39	189.39	0.9999	2.1085	0	2.1085	0.0000	
		GGUF	Q8_0	189.39	189.32	0.9968	14.0268	3.9586	17.9855	0.0026
		Q6_K	189.39	189.18	0.9958	16.0866	12.2537	28.3403	0.0127	
		Q5_K_M	189.39	189.42	0.9934	20.1296	12.2610	32.3906	0.0200	
	BnB	Q4_K_M	189.39	189.59	0.9838	31.6498	12.2579	43.9077	0.0059	
		Q3_K_M	189.39	187.25	0.9604	49.1985	12.1641	61.3626	0.0089	
		Q2_K	189.39	187.79	0.8818	85.0924	12.1339	97.2264	0.1166	
		INT8	189.39	189.26	0.9953	17.0549	0	17.0549	0.0028	
		NF4	189.39	189.84	0.9609	49.2064	0	49.2064	0.0368	
		FP4	189.39	188.99	0.9398	60.9485	0	60.9485	0.0762	
TriviaQA ($r_s=0.95$)	-	FP16	193.86	193.86	1.0000	0.0000	0	0.0000	0.0000	
		GGUF	Q8_0	193.86	193.78	0.9968	14.4438	3.8392	18.2830	0.0083
		Q6_K	193.86	193.70	0.9956	16.8858	11.9492	28.8350	0.0032	
		Q5_K_M	193.86	193.82	0.9932	21.0100	11.9509	32.9609	0.0264	
	BnB	Q4_K_M	193.86	193.86	0.9835	32.6491	11.9489	44.5980	0.0389	
		Q3_K_M	193.86	193.84	0.9510	56.2967	11.9505	68.2472	0.1490	
		Q2_K	193.86	194.74	0.8363	103.1688	11.9755	115.1442	0.5791	
		INT8	193.86	193.95	0.9945	18.8954	0	18.8954	0.0204	
		NF4	193.86	194.07	0.9634	48.7160	0	48.7160	0.0883	
		FP4	193.86	194.53	0.9354	64.7803	0	64.7803	0.1946	
SQuAD ($r_s=0.71$)	-	FP16	184.40	184.40	1.0000	0.0000	0	0.0000	0.0000	
		GGUF	Q8_0	184.40	184.36	0.9973	12.4849	3.7172	16.2022	0.0259
		Q6_K	184.40	184.18	0.9966	14.1879	11.6908	25.8787	0.0033	
		Q5_K_M	184.40	184.34	0.9945	17.9356	11.6952	29.6309	0.0275	
	BnB	Q4_K_M	184.40	184.38	0.9869	27.7450	11.6921	39.4372	0.0112	
		Q3_K_M	184.40	183.81	0.9651	45.1158	11.6797	56.7954	0.0239	
		Q2_K	184.40	184.73	0.8963	78.0052	11.6862	89.6914	0.1217	
		INT8	184.40	184.46	0.9965	14.3850	0	14.3850	0.0187	
		NF4	184.40	184.56	0.9714	40.9475	0	40.9475	0.0661	
		FP4	184.40	185.74	0.9524	53.0345	0	53.0345	0.0804	
GSM8K ($r_s=0.83$)	-	FP16	175.51	175.51	1.0000	0.0000	0	0.0000	0.0000	
		GGUF	Q8_0	175.51	175.44	1.0000	0.0627	3.6483	3.7110	0.0025
		Q6_K	175.51	175.32	1.0000	0.1786	11.5811	11.7597	0.0015	
		Q5_K_M	175.51	175.29	1.0000	0.2011	11.5826	11.7837	0.0032	
	BnB	Q4_K_M	175.51	175.40	1.0000	0.1002	11.5841	11.6843	0.0005	
		Q3_K_M	175.51	174.95	1.0000	0.5201	11.5688	12.0889	0.0100	
		Q2_K	175.51	176.60	0.9848	28.5182	11.6049	40.1231	0.0266	
		INT8	175.51	175.55	1.0000	0.0420	0	0.0420	0.0002	
		NF4	175.51	175.39	1.0000	0.1070	0	0.1070	0.0001	
		FP4	175.51	176.81	1.0000	1.2061	0	1.2061	0.0076	

G Qwen3-8B forgetting and shape-regularization replications

This appendix reports the Qwen3-8B replications of Sec. 5.2 and Sec. 5.4 along with the remaining trace-norm decomposition tables (Llama BBQ and both Qwen fine-tuning tasks). Qwen3-8B differs from Llama-3.1-8B in depth (36 vs. 32 layers), vocabulary size (151,936 vs. 128,256), and pre-training corpus (multilingual, $\sim 36T$ tokens vs. English-dominant, $\sim 15T$ tokens); reproducing the main-text patterns under these shifts provides cross-family evidence for the claims of Secs. 5.2–5.4.

Table 10: Per-benchmark mean empirical risk gap $|\Delta\mathcal{R}|$ (averaged over per-method aggregated quantization rows, matching the per-model body tables) and per-benchmark mean Spearman $r_s(\mathcal{B}, |\Delta\mathcal{R}|)$ (over raw variants, matching the figure’s per-subplot r_s) across seven 8B model families. GSM8K’s small $|\Delta\mathcal{R}|$ —driven by long teacher-forced answer spans diluting per-token loss—yields a low signal-to-noise ratio that depresses its rank correlation.

Model	Empirical risk gap $ \Delta\mathcal{R} $				
	ARC	MMLU	SQuAD	TriviaQA	GSM8K
Llama-3.1-8B	0.0795	0.0812	0.1040	0.1839	0.0311
Ministral-3-8B	0.0870	0.0761	0.0329	0.0711	0.0116
Qwen3-8B	0.1223	0.0896	0.1405	0.1412	0.0470
DeepSeek-R1-8B	0.0899	0.1112	0.1228	0.2680	0.0123
Llama-3.1-8B-Instruct	0.0715	0.1080	0.0721	0.2086	0.0203
Ministral-3-8B-Instruct	0.0282	0.0268	0.0379	0.1108	0.0052
Qwen3-8B-Instruct	0.0334	0.0266	0.0865	0.1559	0.0033
Mean $\Delta\mathcal{R}$	0.0731	0.0742	0.0852	0.1628	0.0187
Mean r_s	0.768	0.793	0.801	0.889	0.405

G.1 Forgetting: bound tracks cross-task drift on Qwen3-8B

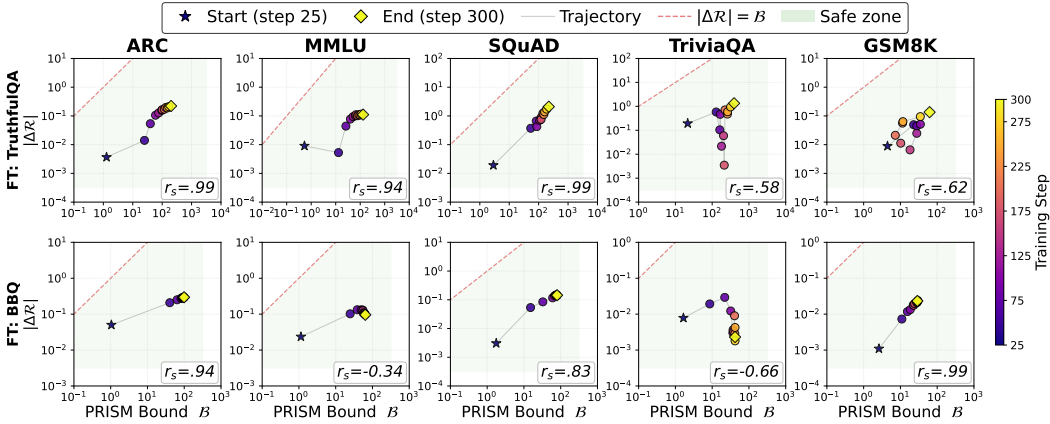


Figure 7: **Qwen3-8B: the PRISM bound tracks catastrophic forgetting across LoRA fine-tuning steps.** Each subplot scatters the PRISM bound tracks \mathcal{B} (x-axis, log) against the empirical forgetting $|\Delta\mathcal{R}|$ (y-axis, log) on a held-out benchmark, with one point per LoRA checkpoint colored by training step. Rows: fine-tuning task (TruthfulQA, BBQ). Columns: held-out evaluation benchmark (ARC, MMLU, SQuAD, TriviaQA, GSM8K). Because LoRA keeps the `lm_head` frozen, the head-discrepancy term γ vanishes and the bound is governed entirely by backbone scale ($\Delta\rho$) and shape ($1 - \Omega$) drift, as predicted by Sec. 4. Spearman r_s per subplot is annotated in each panel. This replicates Fig. 3 on a different family, whose pre-training corpus, depth, and vocabulary size all differ from Llama-3.1-8B.

Figure 7 reproduces the two structural observations of the Llama main-text result (Fig. 3) on Qwen3-8B. First, *the PRISM bound rises in lockstep with empirical forgetting across most (task, benchmark) combinations*: as LoRA fine-tuning proceeds on TruthfulQA or BBQ, $\Omega(Z_0, Z_t)$ drifts away from 1 and ρ_t from ρ_0 , and this backbone drift tracks the empirical cross-entropy drift on most held-out benchmarks—including benchmarks (e.g., GSM8K) whose distributions differ substantially from the fine-tuning data. Second, *different source tasks induce qualitatively different drift geometries*, matching Llama: TruthfulQA fine-tuning drives predominantly shape drift while BBQ moves both scale and shape, a distinction the decomposition of Eq. (7) makes visible whereas a unified distance would collapse it. Because Qwen3-8B differs from Llama-3.1-8B across multiple training and architecture axes (pre-training corpus, depth, vocabulary), this replication is direct evidence that the backbone-drift signal is a cross-family property rather than a Llama-specific artifact.

Per-subplot variability under low-forgetting regimes. A small subset of subplots in Fig. 7—most notably Qwen3-8B fine-tuned on BBQ evaluated on MMLU and TriviaQA—shows weak or slightly

negative per-subplot r_s . These cases share a common signature: $|\Delta\mathcal{R}|$ at $\lambda=0$ sits at order 10^{-3} nats per token—two to three orders of magnitude below the $\sim 10^{-1}$ nat scale at which the bound is informative across the rest of the grid. Within the same (model, fine-tuning task) pair, this is benchmark-specific: Qwen3-8B BBQ at $\lambda=0$ shows $|\Delta\mathcal{R}|\approx 0.0035$ on TriviaQA versus ≈ 0.288 on ARC (Table 21)—roughly two orders of magnitude apart within a single fine-tuning trajectory. When the forgetting magnitude is at this scale, per-checkpoint ranking becomes uninformative; the resulting r_s reflects checkpoint-trajectory noise rather than a failure of the bound. This pattern is a property of the (model, fine-tuning task, benchmark) triple (Qwen3-8B BBQ on TriviaQA is robust to fine-tuning) rather than the diagnostic. The same noise-dominated effect appears in Llama-3.1-8B BBQ \rightarrow SQuAD ($r_s \approx 0.30$, Fig. 3): $|\Delta\mathcal{R}|$ saturates early in fine-tuning, so late checkpoints sit at roughly the same level and the per-checkpoint Spearman is driven by checkpoint noise rather than continued drift.

G.2 Shape regularization: Qwen3-8B replication

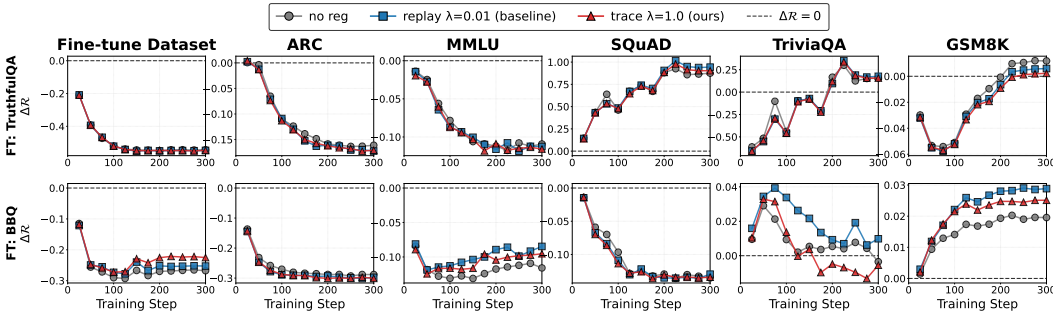


Figure 8: **Shape regularization vs. replay-CE on Qwen3-8B (replication of Fig. 4).** Same three configurations as Llama: *no reg*, *replay* ($\lambda=0.01$), and *trace* ($\lambda=1.0$). Qwen3-8B’s baseline forgetting is already small (mean $|\Delta\mathcal{R}| < 0.27$ on both fine-tuning tasks vs. Llama’s 0.84 on TruthfulQA), leaving little room for improvement; the trace-vs-replay gap narrows accordingly but the qualitative mechanism (trace lifts Ω , replay does not) holds. Per-config decompositions: Tables 20 and 21.

Figure 8 reproduces the main-text Llama comparison (Fig. 4) on Qwen3-8B. Because Qwen3-8B’s baseline forgetting is already small, both methods stay near baseline level; the qualitative pattern (trace contracts Ω , replay does not) holds. Per-config decompositions are in Tables 20 and 21 below.

G.3 Additional trace-norm decomposition tables

Tables 18–21 give the full per-(model, fine-tuning task) decomposition at step 300 for the three configurations (no reg, replay $\lambda=0.01$, trace $\lambda=1.0$); the main-text Table 2 compresses the Llama-TruthfulQA combination to Ω and $|\Delta\mathcal{R}|$ only.

H When shape regularization helps: task-dependence

TruthfulQA-FT, where shape drift dominates downstream forgetting, illustrates the regularizer’s intended use case: trace cuts mean $|\Delta\mathcal{R}|$ from 0.843 (no reg) to 0.681 (−19%), outperforming experience replay (0.764, −9%). BBQ-FT serves as a robustness check in the small- $|\Delta\mathcal{R}|$ regime: averaging the per-benchmark $|\Delta\mathcal{R}|$ values from Table 19 gives means of 0.179 (no reg), 0.195 (trace), and 0.241 (replay)—substantially smaller than TruthfulQA’s 0.843—reflecting BBQ’s modest baseline shape drift (mean baseline $\Omega = 0.932$ vs 0.906). Trace outperforms replay; per-benchmark substantive wins (detailed below) persist on shape-driven cells.

Geometric mechanism remains intact. On BBQ, the contrast between trace and experience replay is most visible in the geometric signal: trace lifts Ω from 0.93 to 0.98 (a 73% reduction in $1 - \Omega$) while experience replay leaves Ω flat (0.93 \rightarrow 0.93). The regularizer’s targeted quantity moves as designed.

Per-benchmark wins on shape-driven cells. Trace’s largest $|\Delta\mathcal{R}|$ reductions appear where forgetting is substantive: on BBQ-FT (Table 19), TriviaQA $|\Delta\mathcal{R}|$ drops from 0.143 to 0.017 (−88%) and GSM8K from 0.061 to 0.013 (−79%); on TruthfulQA-FT (Table 2), SQuAD from 1.337 to 1.054

Table 18: Regularization comparison for **Llama-3.1-8B** fine-tuned on **TruthfulQA** under identity alignment ($W=I$). Rows group by evaluation benchmark; each benchmark block lists metrics at step 300 for: no reg, replay $\lambda=0.01$ (baseline), trace $\lambda=1.0$ (ours). Bold / underline: 1st / 2nd-best smallest $|\Delta\mathcal{R}|$ and largest Ω per block. Shading: $\Omega < 0.80$ / $\Omega < 0.95$ on $(\Omega, \delta, \mathcal{B}, |\Delta\mathcal{R}|)$; $\gamma=0$ under frozen `lm_head`.

Dataset	Method (λ)	ρ_T	ρ_P	Ω	δ	γ	PRISM \mathcal{B}	$ \Delta\mathcal{R} $
ARC	no reg	137.55	137.75	0.9158	147.6081	0	147.6081	0.0290
	replay $\lambda=0.01$ (baseline)	137.55	137.35	<u>0.9185</u>	145.0853	0	145.0853	0.0108
	trace $\lambda=1.0$ (ours)	137.55	137.32	0.9319	132.5490	0	132.5490	0.0199
MMLU	no reg	138.91	139.50	0.9426	123.2722	0	123.2722	0.1339
	replay $\lambda=0.01$ (baseline)	138.91	138.94	<u>0.9451</u>	120.3033	0	120.3033	0.1031
	trace $\lambda=1.0$ (ours)	138.91	139.09	0.9542	109.9868	0	109.9868	<u>0.1116</u>
SQuAD	no reg	138.20	140.07	0.9231	142.6639	0	142.6639	1.3372
	replay $\lambda=0.01$ (baseline)	138.20	139.58	<u>0.9345</u>	131.4408	0	131.4408	<u>1.1911</u>
	trace $\lambda=1.0$ (ours)	138.20	139.04	0.9478	117.0684	0	117.0684	1.0543
TriviaQA	no reg	140.93	146.85	0.7593	261.3595	0	261.3595	2.5829
	replay $\lambda=0.01$ (baseline)	140.93	146.18	<u>0.7810</u>	248.6873	0	248.6873	2.3879
	trace $\lambda=1.0$ (ours)	140.93	145.10	0.8210	223.8704	0	223.8704	2.1242
GSM8K	no reg	137.15	138.32	0.9905	49.6934	0	49.6934	0.1342
	replay $\lambda=0.01$ (baseline)	137.15	138.01	<u>0.9957</u>	33.3099	0	33.3099	<u>0.1261</u>
	trace $\lambda=1.0$ (ours)	137.15	137.65	1.0000	1.3192	0	1.3192	0.0966

Table 19: Regularization comparison for **Llama-3.1-8B** fine-tuned on **BBQ** under identity alignment ($W=I$). Rows group by evaluation benchmark; each benchmark block lists metrics at step 300 for: no reg, replay $\lambda=0.01$ (baseline), trace $\lambda=1.0$ (ours). Bold / underline: 1st / 2nd-best smallest $|\Delta\mathcal{R}|$ and largest Ω per block. Shading: $\Omega < 0.80$ / $\Omega < 0.95$ on $(\Omega, \delta, \mathcal{B}, |\Delta\mathcal{R}|)$; $\gamma=0$ under frozen `lm_head`.

Dataset	Method (λ)	ρ_T	ρ_P	Ω	δ	γ	PRISM \mathcal{B}	$ \Delta\mathcal{R} $
ARC	no reg	137.55	133.78	<u>0.8804</u>	173.7045	0	173.7045	0.0775
	replay $\lambda=0.01$ (baseline)	137.55	135.25	0.8802	174.6273	0	174.6273	0.1799
	trace $\lambda=1.0$ (ours)	137.55	137.06	0.9762	78.3406	0	78.3406	<u>0.1536</u>
MMLU	no reg	138.91	135.04	0.8744	179.6944	0	179.6944	0.3531
	replay $\lambda=0.01$ (baseline)	138.91	136.63	<u>0.8766</u>	178.9974	0	178.9974	0.6061
	trace $\lambda=1.0$ (ours)	138.91	138.66	0.9758	79.8590	0	79.8590	<u>0.4995</u>
SQuAD	no reg	138.20	139.04	0.9281	137.3737	0	137.3737	<u>0.2608</u>
	replay $\lambda=0.01$ (baseline)	138.20	139.16	<u>0.9366</u>	129.0819	0	129.0819	0.2127
	trace $\lambda=1.0$ (ours)	138.20	138.34	0.9694	89.4630	0	89.4630	0.2903
TriviaQA	no reg	140.93	141.47	0.9780	77.4262	0	77.4262	<u>0.1435</u>
	replay $\lambda=0.01$ (baseline)	140.93	141.60	<u>0.9784</u>	76.6896	0	76.6896	0.1506
	trace $\lambda=1.0$ (ours)	140.93	140.99	0.9955	34.9074	0	34.9074	0.0171
GSM8K	no reg	137.15	137.41	1.0000	0.6918	0	0.6918	0.0609
	replay $\lambda=0.01$ (baseline)	137.15	137.41	<u>1.0000</u>	0.6895	0	0.6895	<u>0.0581</u>
	trace $\lambda=1.0$ (ours)	137.15	137.10	1.0000	0.1255	0	0.1255	0.0126

(−21%) and TriviaQA from 2.583 to 2.124 (−18%). On BBQ-FT ARC and MMLU, the no-reg condition shows substantial shape drift (Ω drops to 0.88, 0.87) with relatively small $|\Delta\mathcal{R}|$ (0.077, 0.353): the no-reg evidence indicates shape drift does not translate proportionally into $|\Delta\mathcal{R}|$ growth on these cells, so trace’s shape restoration lacks a proportional $|\Delta\mathcal{R}|$ target. These cells’ shorter answer spans further compress the per-cell CE dynamic range, limiting the observable signal-to-noise of any regularization effect; when absolute $|\Delta\mathcal{R}|$ is small, per-sample CE noise forms a relatively larger fraction of the signal. Rank correlation across the 2×5 grid (Sec. 5.2, mean Spearman ≈ 0.83) provides the scale-invariant calibration of the bound’s predictive power.

When to apply: empirical validation of the gating signal. Shape regularization is indicated when (i) Ω drifts substantially during fine-tuning and (ii) downstream forgetting is shape-dominated; PRISM’s decomposition (Sec. 5.3) provides both signals *before* regularization is applied. To quantify how well the gating prediction matches the empirical trace effect, we compute two per-setting scalars across the four (model, fine-tuning task) combinations, both at step 300 on the same five downstream benchmarks:

Table 20: Regularization comparison for **Qwen3-8B-Base** fine-tuned on **TruthfulQA** under identity alignment ($W=I$). Rows group by evaluation benchmark; each benchmark block lists metrics at step 300 for: no reg, replay $\lambda=0.01$ (baseline), trace $\lambda=1.0$ (ours). Bold / underline: 1st / 2nd-best smallest $|\Delta\mathcal{R}|$ and largest Ω per block. Shading: $\Omega < 0.80$ / $\Omega < 0.95$ on $(\Omega, \delta, \mathcal{B}, |\Delta\mathcal{R}|)$; $\gamma=0$ under frozen `lm_head`.

Dataset	Method (λ)	ρ_T	ρ_P	Ω	δ	γ	PRISM \mathcal{B}	$ \Delta\mathcal{R} $
ARC	no reg	332.98	327.46	<u>0.9963</u>	100.0550	0	100.0550	0.1612
	replay $\lambda=0.01$ (baseline)	332.98	327.21	0.9959	105.4953	0	105.4953	0.1725
	trace $\lambda=1.0$ (ours)	332.98	327.29	0.9965	97.1908	0	97.1908	<u>0.1708</u>
MMLU	no reg	333.53	328.76	0.9984	67.4051	0	67.4051	0.1092
	replay $\lambda=0.01$ (baseline)	333.53	328.53	0.9981	71.7638	0	71.7638	<u>0.1125</u>
	trace $\lambda=1.0$ (ours)	333.53	328.70	0.9985	64.5258	0	64.5258	0.1158
SQuAD	no reg	297.68	292.04	<u>0.9930</u>	122.0758	0	122.0758	0.8757
	replay $\lambda=0.01$ (baseline)	297.68	292.31	0.9926	125.2384	0	125.2384	0.9437
	trace $\lambda=1.0$ (ours)	297.68	293.13	0.9932	120.3011	0	120.3011	<u>0.9025</u>
TriviaQA	no reg	240.42	224.70	<u>0.9667</u>	214.4331	0	214.4331	0.1552
	replay $\lambda=0.01$ (baseline)	240.42	223.97	0.9647	220.7355	0	220.7355	0.1767
	trace $\lambda=1.0$ (ours)	240.42	225.12	0.9674	212.1221	0	212.1221	<u>0.1575</u>
GSM8K	no reg	269.06	271.54	1.0000	8.5518	0	8.5518	0.0118
	replay $\lambda=0.01$ (baseline)	269.06	272.36	<u>1.0000</u>	11.3864	0	11.3864	<u>0.0060</u>
	trace $\lambda=1.0$ (ours)	269.06	272.50	1.0000	11.8835	0	11.8835	0.0023

Table 21: Regularization comparison for **Qwen3-8B-Base** fine-tuned on **BBQ** under identity alignment ($W=I$). Rows group by evaluation benchmark; each benchmark block lists metrics at step 300 for: no reg, replay $\lambda=0.01$ (baseline), trace $\lambda=1.0$ (ours). Bold / underline: 1st / 2nd-best smallest $|\Delta\mathcal{R}|$ and largest Ω per block. Shading: $\Omega < 0.80$ / $\Omega < 0.95$ on $(\Omega, \delta, \mathcal{B}, |\Delta\mathcal{R}|)$; $\gamma=0$ under frozen `lm_head`.

Dataset	Method (λ)	ρ_T	ρ_P	Ω	δ	γ	PRISM \mathcal{B}	$ \Delta\mathcal{R} $
ARC	no reg	332.98	325.46	<u>0.9976</u>	82.4401	0	82.4401	0.2881
	replay $\lambda=0.01$ (baseline)	332.98	324.38	0.9967	96.6146	0	96.6146	<u>0.2975</u>
	trace $\lambda=1.0$ (ours)	332.98	327.55	0.9987	60.7069	0	60.7069	0.3009
MMLU	no reg	333.53	328.73	0.9991	52.3490	0	52.3490	0.1159
	replay $\lambda=0.01$ (baseline)	333.53	328.17	0.9987	61.9216	0	61.9216	0.0847
	trace $\lambda=1.0$ (ours)	333.53	330.08	0.9992	46.8071	0	46.8071	<u>0.0954</u>
SQuAD	no reg	297.68	286.65	<u>0.9985</u>	67.1415	0	67.1415	0.1353
	replay $\lambda=0.01$ (baseline)	297.68	285.88	0.9982	72.9559	0	72.9559	0.1296
	trace $\lambda=1.0$ (ours)	297.68	287.67	0.9991	55.9438	0	55.9438	<u>0.1342</u>
TriviaQA	no reg	240.42	235.59	<u>0.9992</u>	36.1152	0	36.1152	0.0035
	replay $\lambda=0.01$ (baseline)	240.42	235.16	0.9989	42.8307	0	42.8307	0.0098
	trace $\lambda=1.0$ (ours)	240.42	236.13	0.9994	33.0855	0	33.0855	<u>0.0055</u>
GSM8K	no reg	269.06	261.82	1.0000	25.0486	0	25.0486	0.0196
	replay $\lambda=0.01$ (baseline)	269.06	260.60	<u>1.0000</u>	29.2693	0	29.2693	0.0288
	trace $\lambda=1.0$ (ours)	269.06	262.96	1.0000	21.1073	0	21.1073	<u>0.0251</u>

- **Baseline shape-drift signal** $1-\bar{\Omega} := \frac{1}{5} \sum_b (1 - \Omega_b^{\lambda=0})$, the across-benchmark mean shape mismatch under no regularization, with per-benchmark $\Omega_b^{\lambda=0}$ read from the no-reg rows of Tables 18–21. Larger $1-\bar{\Omega}$ = larger headroom under condition (i).
- **Relative trace effect** $\Delta|\Delta\mathcal{R}|/|\Delta\mathcal{R}|_0 := (|\Delta\mathcal{R}|_{\text{trace}} - |\Delta\mathcal{R}|_{\lambda=0})/|\Delta\mathcal{R}|_{\lambda=0}$: across-benchmark mean of the trace-vs-no-reg relative change in empirical forgetting at $\lambda=1.0$ (negative = trace helps; positive = trace hurts).

Three of four settings match the gating prediction directly: trace produces the largest benefit where $1-\bar{\Omega}$ is largest (Llama TruthfulQA: -19.2%), and is essentially neutral (magnitude $< 3\%$) on both Qwen settings where $1-\bar{\Omega}$ sits at the noise floor. Llama BBQ is the partial exception—its aggregate $1-\bar{\Omega} = 0.0678$ exceeds the noise floor (condition (i) satisfied), but the drift is concentrated on ARC and MMLU where condition (ii) is violated: substantial shape drift accompanies small $|\Delta\mathcal{R}|$ growth, so trace’s shape restoration lacks a proportional $|\Delta\mathcal{R}|$ target (per-benchmark paragraph above). On the two Llama-BBQ benchmarks where condition (ii) does hold (TriviaQA and GSM8K), trace

Table 22: Diagnostic-gating prediction vs. empirical trace effect across the four (model, fine-tuning task) settings, ordered by decreasing $1-\bar{\Omega}$. Trace yields the largest $|\Delta\mathcal{R}|$ reduction where shape drift is largest (Llama TruthfulQA), is essentially neutral on both Qwen settings where $1-\bar{\Omega}$ sits at the noise floor, and shows a partial cell-level exception on Llama BBQ explained in the next paragraph.

Setting	$1-\bar{\Omega}$	$\Delta \Delta\mathcal{R} / \Delta\mathcal{R} _0$	Gating verdict
Llama TruthfulQA	0.0937	-19.2%	shape-driven \Rightarrow apply
Llama BBQ	0.0678	+8.6%	cell-level mixed (see below)
Qwen TruthfulQA	0.0091	+2.7%	at noise floor \Rightarrow skip
Qwen BBQ	0.0011	-0.2%	at noise floor \Rightarrow skip

yields -88% and -79% reductions respectively, so the aggregate +8.6% reflects mixed cell-level behavior rather than a failure of the shape-drift gating itself. Adaptive per-cell deployment of the regularizer—driven by PRISM’s per-benchmark decomposition online—is the natural extension and is left to future work, alongside the short-answer fine-tuning regimes noted earlier in this appendix.

Empirical confirmation: Qwen3-8B replication. The Qwen3-8B replication (Tables 20–21, Fig. 8) extends the regime-dependence story from *tasks* (TruthfulQA-FT vs. BBQ-FT on Llama) to *models*, providing direct empirical evidence for condition (i) above. Qwen3-8B is markedly more robust to LoRA forgetting on these two fine-tuning sources than Llama-3.1-8B: across-benchmark mean $|\Delta\mathcal{R}|$ at $\lambda=0$ is 0.263 on Qwen TruthfulQA-FT vs. Llama’s 0.843 (3.2 \times smaller), and 0.112 on Qwen BBQ-FT vs. Llama’s 0.179. Baseline shape preservation is correspondingly closer to its ceiling on Qwen (Ω at $\lambda=0$: 0.991 on Qwen TruthfulQA-FT, 0.999 on Qwen BBQ-FT vs. Llama’s 0.906 and 0.932), leaving the shape regularizer with essentially no drift to repair: $1-\Omega$ collapses from Llama’s 0.094/0.068 to Qwen’s 0.009/0.001, an order of magnitude smaller. The differences across no-reg, replay, and trace correspondingly shrink to the evaluation-noise floor: across-benchmark mean $|\Delta\mathcal{R}|$ on Qwen TruthfulQA-FT is 0.263 / 0.282 / 0.270 (no-reg / replay / trace), and on Qwen BBQ-FT is 0.112 / 0.110 / 0.112, with method-to-method spread under 0.02 on both. This is the same low-SNR phenomenon documented for GSM8K under PTQ in Appendix F.3 (Table 10), where the bound’s per-benchmark mean Spearman drops from ≥ 0.77 on ARC/MMLU/SQuAD/TriviaQA to ≈ 0.41 on GSM8K precisely because $|\Delta\mathcal{R}|$ collapses to ≈ 0.019 . We report the Qwen3-8B regularization numbers in full for transparency and reproducibility, but emphasize that the shape regularizer’s mechanism—contracting $1-\Omega$ at the source of LoRA backbone drift—can demonstrate a measurable benefit only when $1-\Omega$ has substantive headroom to contract. Qwen3-8B fine-tuning on TruthfulQA/BBQ violates condition (i) above, and the Qwen3-8B numbers therefore do not contradict the Llama TruthfulQA-FT result; they confirm the regime-dependence the bound itself predicts.

I Future work

- **Beyond LoRA forgetting.** PRISM’s diagnostic and regularization roles (Sec. 5.4) extend naturally to broader fine-tuning—full SFT, distillation, continual learning—where backbone drift is substantially larger. The shape regularizer constrains drift; Ω and $\Delta\rho$ together monitor it per step in ways validation loss does not.
- **Diagnostic applications.** The single-forward-pass computation of \mathcal{B} enables three deployment uses: *per-sample OOD detection* via scale and shape residuals on individual inputs; *cross-scale hyperparameter transfer* between a small proxy and its scaled target to predict tuning robustness; and *production drift monitoring* on live traffic.
- **Beyond LLMs.** Vision Transformers and contrastive image encoders share LLMs’ backbone-then-linear-head structure, with final-layer LayerNorm (and strict L2 normalization in CLIP/SigLIP) enforcing tight feature scales—making the PRISM scale axis naturally small. Natural targets include ViT quantization, vision-encoder distillation, and cross-modal alignment (consistent with the Platonic Representation Hypothesis [16]).